RESEARCH ARTICLE

Spatially Segregated Macrophage Populations Predict Distinct Outcomes in Colon Cancer

Magdalena Matusiak[1], John W. Hickey[1], David G.P. van IJzendoorn[1], Guolan Lu[1], Lukasz Kidziński[4], Shirley Zhu[1], Deana R.C. Colburg[1], Bogdan Luca[2,3], Darci J. Phillips[1], Sky W. Brubaker[5], Gregory W. Charville[1], Jeanne Shen[1], Kyle M. Loh[6,7], Derick K. Okwan-Duodu[1], Garry P. Nolan[1], Aaron M. Newman[3,7,8], Robert B. West[1], and Matt van de Rijn[1]

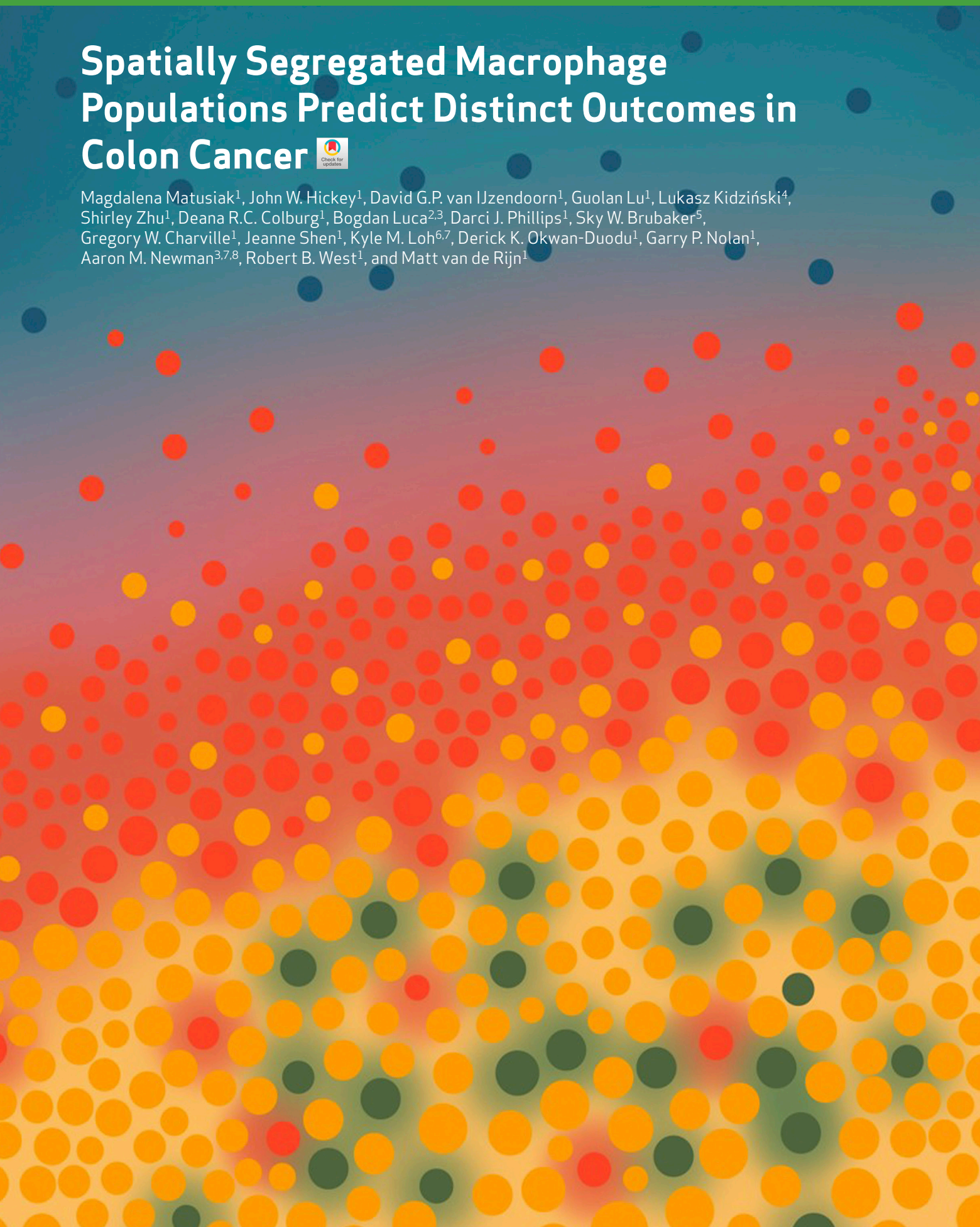

ABSTRACT Tumor-associated macrophages are transcriptionally heterogeneous, but the spatial distribution and cell interactions that shape macrophage tissue roles remain poorly characterized. Here, we spatially resolve five distinct human macrophage populations in normal and malignant human breast and colon tissue and reveal their cellular associations. This spatial map reveals that distinct macrophage populations reside in spatially segregated micro-environmental niches with conserved cellular compositions that are repeated across healthy and diseased tissue. We show that IL4I1$^+$ macrophages phagocytose dying cells in areas with high cell turnover and predict good outcome in colon cancer. In contrast, SPP1$^+$ macrophages are enriched in hypoxic and necrotic tumor regions and portend worse outcome in colon cancer. A subset of FOLR2$^+$ macrophages is embedded in plasma cell niches. NLRP3$^+$ macrophages co-localize with neutrophils and activate an inflammasome in tumors. Our findings indicate that a limited number of unique human macrophage niches function as fundamental building blocks in tissue.

SIGNIFICANCE: This work broadens our understanding of the distinct roles different macrophage populations may exert on cancer growth and reveals potential predictive markers and macrophage population-specific therapy targets.

INTRODUCTION

As sentinel immune cells within tissues, macrophages execute diverse roles including pathogen defense, antigen presentation, phagocytosis of dying cells, and secretion of signals that drive tissue repair (1–3). Macrophages also play important roles in tumors, as evidenced by the fact that their infiltration within tumors predict poor patient outcomes for most tumor types (4). As a result, tumor-associated macrophages (TAMs) were surmised to be a promising cancer therapy target. However, single agents targeting TAMs (e.g., CSF1 pathway inhibitors) have thus far shown minimal efficacy against solid tumors (5, 6). This may be in part because such therapies monolithically repress macrophages without consideration for their heterogeneity. Clearly, a better understanding of the molecular and functional diversity of macrophages is needed to facilitate rational macrophage targeting in cancer and to predict clinical outcomes.

Defining molecular diversity of macrophage subsets and their spatial organization relative to one another, and other cells within tissues, is a preeminent goal of immunology. It has long been appreciated that macrophages residing in different tissues are different from one another, reflecting tissue specializations (7, 8). More recently, attention has turned to whether even macrophages within a single tissue exhibit diversity (9). For instance, two subsets of LYVE1^{lo} MHC-II^{hi} versus LYVE1^{hi} MHC-II^{lo} macrophages have been identified in several mouse tissues (10). Another study identified two macrophage subsets in human colon: one ACP5$^+$ C1Q$^+$ macrophages in lamina propria (LP) and second, LYVE1$^+$ COLEC12$^+$, in colon submucosa (11). Transcriptional macrophage heterogeneity is also apparent in human cancer and murine models of cancer (12–15). Yet, a comprehensive spatial organization of the putative tumor–associated macrophage subsets remains to be profiled.

As a prelude to understanding spatial interactions of macrophage subtypes with other cells and their impact on cancer outcomes, we and others used immunostaining to show differential spatial enrichment of specific macrophage populations with distinct T cell or fibroblast subtypes (16–19). However, those studies were limited to examining at most one or two distinct macrophage populations and one other cell type at a time in a single organ. Unbiased and highly multiplexed profiling across all cell types within a given organ, and across multiple organs, is needed to dissect the spatial organization of macrophages within a tissue, as well as cell–cell interactions that shape macrophage roles in the tumor microenvironment (TME).

Here we employ multiplexed protein analyses to define five human macrophage populations (LYVE1$^+$, FOLR2$^+$, IL4I1$^+$, NLRP3$^+$, and SPP1$^+$ macrophages) and to spatially map their distributions within human breast and intestinal tissues, as well as their malignant counterparts (breast cancer and colorectal cancer). An important aspect of our approach is that we also simultaneously stain other cell types in the tissue, providing a comprehensive insight into the multicellular environments that these macrophage populations inhabit. To our surprise, these

[1]Department of Pathology, Stanford University, Stanford, California. [2]Department of Medicine, Stanford Center for Biomedical Informatics Research, Stanford University, Stanford, California. [3]Department of Biomedical Data Science, Stanford University, Stanford, California. [4]Department of Bioengineering, Stanford University, Stanford, California. [5]Department of Microbiology and Immunology, Stanford University, Stanford, California. [6]Department of Developmental Biology, Stanford University, Stanford, California. [7]Institute for Stem Cell Biology and Regenerative Medicine, Stanford University, Stanford, California. [8]Stanford Cancer Institute, Stanford University, Stanford, California.

Corresponding Authors: Magdalena Matusiak, Department of Pathology, Stanford University, 300 Pasteur Drive, Room L209, Stanford, CA 94305. E-mail: mmatusia@stanford.edu; and Matt van de Rijn, mrijn@stanford.edu

Cancer Discov 2024;14:1418–39

doi: 10.1158/2159-8290.CD-23-1300

five macrophage populations were not randomly distributed throughout tissues. Rather, they occupied spatially distinct niches characterized by unique cellular compositions, discrete histological properties, and conferred distinct effects on human patients' outcomes. The LYVE1$^+$ and FOLR2$^+$ macrophage populations were conserved across both human breast and intestine tissues, with a subset of FOLR2$^+$ tissue resident macrophages (TRMs) enriched in the plasma cell niche. IL4I1$^+$ macrophages were present in regions exhibiting high cell turnover in both healthy and cancerous tissues where they were engaged in efferocytosis. This population correlated with anti-PD1 treatment response in breast cancer and favorable outcome in patients with colorectal cancer. The SPP1$^+$ and NLRP3$^+$ macrophages only emerged in diseased tissue. SPP1$^+$ macrophages were associated with hypoxia and tumor necrosis and predicted poor outcome in patients with colorectal cancer. Furthermore, NLRP3$^+$ macrophages harboring active inflammasomes were spatially associated with infiltrating neutrophils across breast cancer, colorectal cancer, and Crohn's disease (CD), suggesting that inflammasome activation contributes to neutrophil tissue accumulation.

To foster widespread accessibility to the wealth of images acquired in this work, we have developed a cloud-based image viewer. Overcoming barriers of entry for nonexperts, it operates effortlessly in web browsers, eliminating the need for extensive computational resources and coding expertise. By accepting standard tiff images and employing efficient preprocessing, the IF Viewer enables swift and intuitive exploration for researchers and nonexperts alike, offering an invaluable visual resource for comprehending the scope of our findings.

Taken together, our work reveals an elaborate spatially organized network of five different macrophage populations embedded in distinct tissue niches. As we show that the existence of these macrophage populations, and their surrounding niches, are conserved across multiple organs and clinical tissue states (healthy, cancerous, and inflamed), this work conceptualizes the macrophage niche as a fundamental and conserved tissue building block. Importantly, we establish clinical-grade antibodies to identify these human macrophage populations, enabling laboratories worldwide to define distinct macrophage populations *in situ* in human clinical specimens. We demonstrate strategies to identify new candidate predictive and prognostic markers and macrophage-targeted cancer therapy targets. Finally, we provide an online resource (https://magdalenamat.github.io/Spatial_MAC_Map/) to enable easy exploration and downloading of images acquired during this study.

RESULTS

Experimental Approach

This work aimed to reveal the spatial distribution of distinct human macrophage subsets and the cellular composition of their respective niches. We focused on breast cancer and colorectal cancer because macrophage abundance (as assessed by CD68 staining) predicts the opposite clinical outcomes in patients with breast cancer and colorectal cancer (4, 20). High CD68 macrophage infiltration was associated with bad outcome in breast cancer but good outcome in colorectal cancer. We thus hypothesized that comparing breast cancer to colorectal cancer macrophages might reveal clinical markers associated with different macrophage functional polarization states. We used four public scRNAseq datasets of colorectal cancer and breast cancer (21–23) to discover markers of distinct macrophage subtypes (Fig. 1A) and established a panel of six antibodies that are compatible with formalin-fixed, paraffin-embedded (FFPE) tissue. These antibodies identified five discrete macrophage populations *in situ*. We subsequently used whole section IHC, four-color immunofluorescence (IF), and 36-antibody CODEX assays on tissue microarrays (TMAs) to discover distinct spatial macrophage niches and the possible functions these spatially resolved TAM subsets fulfill in the TME and as TRM in normal tissue (Fig. 1B, results in Figs. 2–6). In addition, we used CosMx protein profiling to characterize macrophage subset immune polarization in more detail. Figure references with "v" prefix link to IF images of large regions of the entire conventional paraffin sections imaged and are frequently accompanied by additional images showing the same phenomenon across different patients.

Identification of Macrophage Subset Markers by Single-cell RNA Sequencing

To discover markers of different macrophage populations, we integrated, clustered, and compared monocyte and macrophage scRNAseq data spanning 18,698 cells from 128 samples derived from 92 patients across four published studies of breast cancer and colorectal cancer (Fig. 1A and C; Supplementary Fig. S1A). We defined 11 transcriptional clusters marked by differential enrichment of genes and differentiated three monocytes, five TAM, and three TRM subsets (Fig. 1C and D). We selected a clustering resolution that separated known myeloid subtypes as follows: TRMs (*LYVE1*$^+$) form TAMs (*TREM2*$^+$*APOE*$^+$), and patrolling (*CDKN1C*$^+$*FCGR3A*$^+$) from classical monocytes (*VCAN*$^+$*S100A8*$^+$*S100A9*$^+$). We discovered three novel TRM subsets: (i) *LYVE1*$^-$*FOLR2*$^+$ *TRMsFOLR2*$^+$*APOE*$^+$*TREM2*$^+$), (ii) *LYVE1*$^+$*FOLR2*$^+$ *TRMs* (*FOLR2*$^+$ *LYVE1*$^+$ *MARCO*$^+$ *SLC40A1*$^+$ *SEPP1*$^+$), and (iii) *C3*$^+$ *TRMs* (*C3*$^+$*CX3CR1*$^+$), in addition to four previously identified subsets (14, 15, 22), including (iv) *NLRP3*$^+$ *TAMs* (*NLRP3*$^+$ *IL1B*$^+$), (v) *SPP1*$^+$ *TAMs* (*SPP1*$^+$*CHI3L1*$^+$*MT1G*$^+$), (vi) *CXCL9*$^+$ *TAMs* (*CXCL9*$^+$*IL4I1*$^+$), and (vii) *ISG15*$^+$ *TAMs* (*ISG15*$^+$*CXCL10*$^+$*CXCL11*$^+$; Fig. 1D).

The existence of two distinct *FOLR2*$^+$ *TRM* subsets has not been previously reported. Differential gene expression to compare these two subsets showed that *FOLR2*$^+$*LYVE1*$^+$ *TRMs* were enriched in scavenger receptors (*MARCO*, *CD36*, *MRC1*), metabolic enzymes (*BLVRB*, *PDK4*), and immunoglobulins

Figure 1. Identification of macrophage subset markers by single-cell RNA sequencing. **A** and **B,** Flow charts of experimental design. **C,** UMAP projection of monocyte and macrophage scRNA transcriptomes from four studies colored by annotated populations (left) and a breakdown of cells, samples, and patient numbers by study (right). **D,** Dotplot of average marker gene expression per scRNA myeloid population. Highlighted in bold are six markers for which FFPE-compatible antibodies were identified. **E,** Volcano plot shows top differentially expressed genes between FOLR2$^+$, LYVE1$^-$ and FOLR2$^+$, LYVE1$^+$ TRMs. **F,** Barplot of the ratio of $\log_2$ average fractional scRNA myeloid population enrichment between colorectal cancer and breast cancer in tumor samples with more than 35 monocytes and macrophages detected. **G,** Immunofluorescence images show overlap of the established FFPE antibodies and CD68, confirming their reactivity with macrophages.

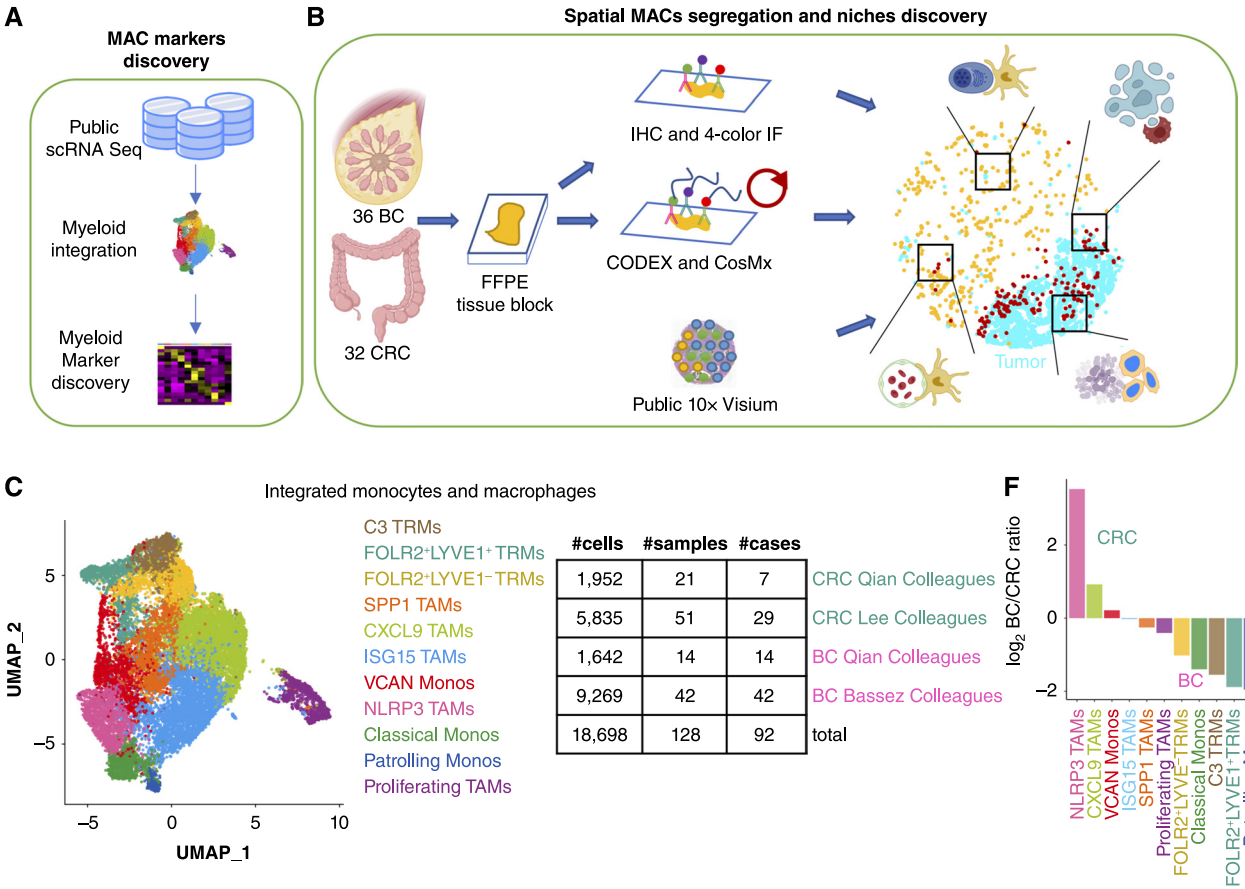
A
MAC markers discovery
Public scRNA Seq
Myeloid integration
Myeloid Marker discovery
B
Spatial MACs segregation and niches discovery
36 BC
32 CRC
FFPE tissue block
IHC and 4-color IF
CODEX and CosMx
Public 10× Visium
Tumor
C
Integrated monocytes and macrophages
UMAP_1
UMAP_2
C3 TRMs
FOLR2+LYVE1+ TRMs
FOLR2+LYVE1− TRMs
SPP1 TAMs
CXCL9 TAMs
ISG15 TAMs
VCAN Monos
NLRP3 TAMs
Classical Monos
Patrolling Monos
Proliferating TAMs
#cells #samples #cases
1,952 21 7 CRC Qian Colleagues
5,835 51 29 CRC Lee Colleagues
1,642 14 14 BC Qian Colleagues
9,269 42 42 BC Bassez Colleagues
18,698 128 92 total
F
log2 BC/CRC ratio
CRC
BC
NLRP3 TAMs
CXCL9 TAMs
VCAN Monos
ISG15 TAMs
SPP1 TAMs
Proliferating TAMs
FOLR2+LYVE−TRMs
Classical Monos
C3 TRMs
FOLR2+LYVE1+TRMs
Patrolling Monos
D
Average expression in cluster
average expr
% Expressed
CDKN1C FCGR3A VCAN FCN1 S100A8 S100A9 NLRP3 IL1B SPP1 CHI3L1 MT1G CXCL10 CXCL11 ISG15 CSCL9 IL4I1 C1QA APOE TREM2 FOLR2 LYVE1 MARCO C3 CX3CR1 MKI67
E
−log10(p.adj)
Avg Log2 Fold Change
FOLR2+LYVE1− TRMs
FOLR2+LYVE1+ TRMs
CD9 CAPG C3 CD74 APOE HLA-DQB1 NUPR1 TRBM2 S100A11 APOC1 FCGR3A HLA-DRB5 SPP1 FN1 LYVE1 BLVRB IGHA1 CD36 PDK4 SELENOP JCHAIN IGKC FOLR2 F13A1 CST3 FCGRT MARCO MRC1 IGLC2 SLC40A1
G
CD68 IL4I1 CRC center of the tumor
CD68 SPP1 CRC invasive front
CD68 NLRP3 BC
CD68 FOLR2 CRC adjacent normal
CD68 LYVE1 normal breast
CD68 MARCO normal breast
20μm

(*IGHA1*, *IGKC*, *IGLC2*). On the other hand, the *FOLR2*$^+$*LYVE1*$^-$ subset was enriched in phagocytosis and antigen presentation gene signatures, further supporting the distinct phenotypes of the two *FOLR2*-positive populations (Fig. 1E).

To explore the distribution of these subsets between colorectal cancer and breast cancer, we computed a ratio of their average frequency across samples with more than 35 myeloid cells. *CXCL9*$^+$ *TAMs* were the most abundant TAM population in both breast cancer and colorectal cancer, and *NLRP3*$^+$ *TAMs* were enriched in colorectal cancer, with about 3.5 $\log_2$ fold higher frequency than in breast cancer (Fig. 1F; Supplementary Fig. S1B–S1D). We also observed fundamental cluster segregation between benign colon and tumor tissue: *NLRP3*$^+$ *TAMs* and *SPP1*$^+$ *TAMs* were almost exclusively confined to colon tumors, whereas *LYVE1*$^+$ *TRMs* were most enriched in benign colon (Supplementary Fig. S1E–S1G). Guided by the above scRNAseq analysis (Fig. 1D; Supplementary Fig. S1E–S1G), we built a panel of commercially available FFPE-compatible antibodies for six macrophage markers to resolve both TAM and TRM populations on the basis of IL4I1, NLRP3, SPP1, FOLR2, LYVE1, and MARCO protein expression (Fig. 1G). The following sections describe how we used these markers to discriminate spatial macrophage niches (Figs. 2 and 3) and to define their cellular composition and propose their functional roles (Figs. 4–7). For clarity, we italicized the names of scRNAseq subsets and refer to cell subsets defined based on protein expression with regular nonitalic font through the text.

FOLR2, IL4I1, NLRP3, and SPP1 Mark Spatially Distinct Macrophage Niches in the TME

To study the spatial distribution of macrophage markers in the TME of breast and colon cancer, we used CD68 and CD163 as canonical macrophage markers, IL4I1, NLRP3, and SPP1 to differentiate TAM populations and FOLR2 to highlight TRMs. ScRNAseq indicated that *NLRP3* is a specific *NLRP3*$^+$ *TAM* marker, *SPP1* is a specific *SPP1*$^+$ *TAM* marker, but *IL4I1* has a broader expression, highlighting *SPP1*$^+$ *TAMs*, *CXCL9*$^+$ *TAMs*, and *ISG15*$^+$ *TAMs*. Nevertheless, the combination of IL4I1, SPP1, and NLRP3 antibodies was sufficient to detect and discriminate NLRP3$^+$ TAMs, SPP1$^+$ TAMs, and IL4I1$^+$ TAM groups (encompassing *ISG15*$^+$ and *CXCL9*$^+$ *TAMs* that we could not resolve) that together labels all scRNA TAMs subsets. In addition, scRNAseq suggested that *SPP1*- and *IL4I1*-expressing populations are enriched in *CD68* gene expression and *FOLR2*$^+$*LYVE1*$^-$ and *FOLR2*$^+$*LYVE1*$^+$ TRM populations are enriched in *CD163* gene expression (Fig. 2A).

We quantified distance from every detected macrophage to its closest tumor cell across a large number of regions and patient samples (Fig. 2B and C), and the four panels in Fig. 2D–G show staining results of macrophage distribution in a single representative 1.5 mm^2 tissue region of human breast cancer and colorectal cancer. Each panel shows (i) an IF image of the discussed markers (left), (ii) a corresponding dotplot representing the spatial macrophage distribution in the TMA core as revealed by the IF (top right), and (iii) a corresponding distance quantification from each detected macrophage to the closest tumor cell in that specimen (bottom right). We started by analyzing the spatial distribution of CD68 and CD163 (Fig. 2B and D, v2D). A commonly held view is that CD163-positive macrophages are of M2 type that help tumor growth and metastasis (24) and are expected to localize close to tumor cells. Surprisingly, contrary to this view, we found that macrophages with higher CD163 expression localized further away from the tumor nests (Fig. 2B and D i, with an average distance of 74.5 μm) compared to macrophages with higher CD68 expression that infiltrated and tightly surrounded the tumor nests (Fig. 2B and D ii, with an average distance of average 35.9 μm).

Next, we interrogated the spatial distribution of FOLR2, IL4I1, NLRP3, and SPP1 in breast cancer and colorectal cancer. We found remarkable and unexpected segregation of these markers where FOLR2 expression was associated with benign tissue localized further away from the tumor (Fig. 2E–G) spatially corresponding to the macrophages with higher CD163 expression (Fig. 2D i). In contrast, macrophages expressing IL4I1 (Fig. 2E, v2E, vBC1t, vBC1b, vBC2), NLRP3 (Fig. 2F, v2F), and SPP1 (Fig. 2G, v2G, vBC1t, vBC1b, vBC2, vBC3, vBC4l, vBC4r, vCRC1, vCRC2, vCRC3, vCRC4l, vCRC4r, vNC) were concentrated immediately adjacent to tumor cells, spatially reflecting the macrophages with higher CD68 expression (Fig. 2D ii). This was confirmed by a distance comparison that analyzed 36,041 macrophages spanning 60 distinct 1.5 mm^2 tissue fragments derived from 14 colorectal cancer to 13 breast cancer cases. This analysis showed that IL4I1$^+$ TAMs were located an average of 38.3 μm away from the closest tumor cell, NLRP3$^+$ TAMs 47.4 μm, SPP1$^+$ TAMs 36.4 μm, while in contrast, FOLR2$^+$ TRMs were located 109 μm from the nearest tumor cell (Fig. 2C).

As we found remarkable spatial segregation of IL4I1$^+$ TAMs and FOLR2$^+$ TRMs in the TME (Fig. 2C and E) in primary tumors, we sought to investigate whether this pattern is conserved in metastatic lesions. We compared IF staining of a colorectal cancer invasive front and a lymph node colorectal cancer, and breast cancer metastasis. Similar to the invasive front of the colorectal cancer tumor (Supplementary Fig. S2A and S2B, vS2A, vS2B), in the lymph node (LN) colorectal cancer metastasis (Supplementary Fig. S2C and S2D, vS2C, vS2D) and breast cancer metastasis (Supplementary Fig. S2E and S2F, vS2E, vS2F), IL4I1$^+$ macrophages were present in the desmoplastic stroma surrounding the tumor nests, and FOLR2$^+$ macrophages were present further away in the surrounding

Figure 2. FOLR2, IL4I1, NLRP3, and SPP1 mark spatially distinct macrophage niches in the TME. **A,** Dotplot shows average macrophage marker expression in scRNA macrophage populations and indicates which scRNA macrophage populations are detectable in four-color IF staining by anti-NLRP3, -SPP1, -IL4I1, -FOLR2, and a combination of anti-FOLR2, -LYVE1, and -MARCO antibodies. **B,** Distance (μm) of CD68 and CD63 macrophages to the closest tumor cell. **C,** Distance (μm) of IL4I1 TAMs, NLRP3 TAMs, SPP1 TAMs, FOLR2 TAMs to the closest tumor cell. **B** and **C,** Cells were identified on CODEX images, *P* values were calculated with a linear mixed-effect model with Bonferroni's corrections for multiple comparisons. **D–G,** Left: CODEX image (**D**) or Immunofluorescence (IF) images (**E–G**) show the distribution of CD68 and CD163 (**D**), or FOLR2 and IL4I1 (**E**), NLRP3 (**F**), SPP1 (**G**) protein expression in representative cases of colorectal cancer (**D**, **E, G**) and breast cancer (**F**). PanCK marks tumor cells. Close-up images on the (bottom) correspond to boxed regions on the (top). Top right: Scatterplots show the distribution of CD68 Macs, CD163 Macs, FOLR2 TRMs, IL4I1 TAMs, NLRP3 TAMs, SPP1 TAMs corresponding to IF images on the (left). Bottom right: Boxplots show the distance quantification of each macrophage to the closest tumor cell corresponding cells identified on IF images on the (left). Pairwise comparisons were determined using a two-sided Wilcoxon rank-sum test on 1,092 (**D**) 580 (**E**), 739 (**F**), and 203 (**G**) cells.

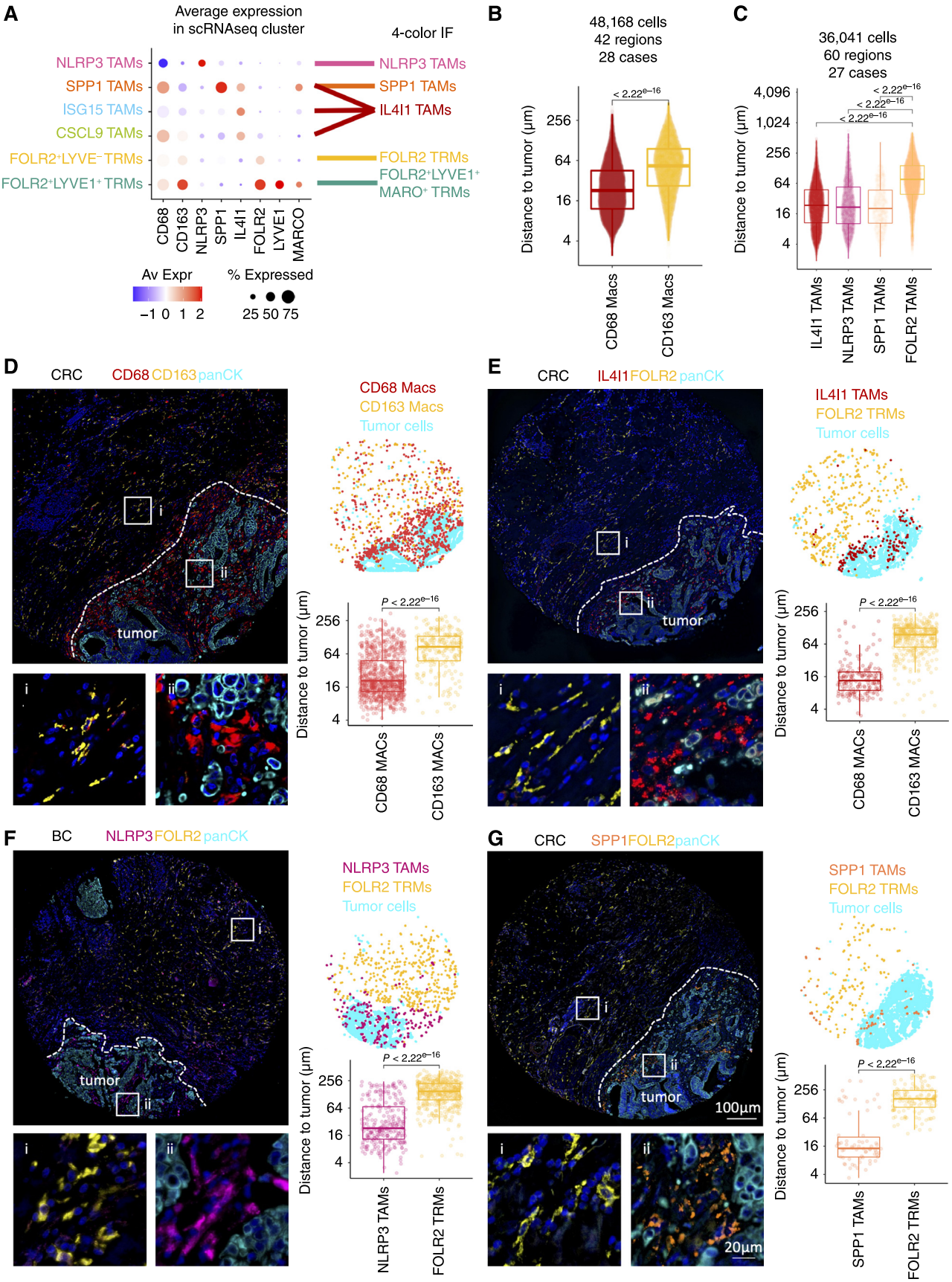
A
Average expression in scRNAseq cluster
4-color IF
NLRP3 TAMs
SPP1 TAMs
ISG15 TAMs
CSCL9 TAMs
FOLR2+LYVE− TRMs
FOLR2+LYVE1+ TRMs
IL4I1 TAMs
FOLR2 TRMs
FOLR2+LYVE1+ MARO+ TRMs
CD68 CD163 NLRP3 SPP1 IL4I1 FOLR2 LYVE1 MARCO
Av Expr
−1 0 1 2
% Expressed
25 50 75
B
48,168 cells
42 regions
28 cases
Distance to tumor (μm)
256 64 16 4
< 2.22e−16
CD68 Macs
CD163 Macs
C
36,041 cells
60 regions
27 cases
Distance to tumor (μm)
4,096 1,024 256 64 16 4
< 2.22e−16
IL4I1 TAMs
NLRP3 TAMs
SPP1 TAMs
FOLR2 TAMs
D
CRC CD68 CD163 panCK
tumor
i
ii
CD68 Macs
CD163 Macs
Tumor cells
P < 2.22e−16
Distance to tumor (μm)
CD68 MACs
CD163 MACs
E
CRC IL4I1 FOLR2 panCK
IL4I1 TAMs
FOLR2 TRMs
Tumor cells
F
BC NLRP3 FOLR2 panCK
NLRP3 TAMs
FOLR2 TRMs
Tumor cells
G
CRC SPP1 FOLR2 panCK
SPP1 TAMs
FOLR2 TRMs
Tumor cells
100μm
20μm

benign tissue. This suggests that the presence of the tumor shapes macrophage phenotype and distribution in the TME in a similar way independent of the tumor type (breast cancer and colorectal cancer share the same TAM populations) or whether the tumor is primary or metastatic. In addition, we report that a thin buffer zone of macrophages coexpressing both FOLR2 and IL4I1 existed in both primary tumor and metastasis specimens (Supplementary Fig. S2A–S2F).

To verify whether the spatial separation of IL4I1$^+$ TAMs and FOLR2$^+$ TRMs in the TME occurs across other human tumors we extended our analysis to additionally profile two major cancer subtypes (adenocarcinomas and squamous cell carcinomas) spanning eight different organs of origin: cheek skin, oral mucosa, larynx, esophagus, lung, stomach, pancreas, and bladder (Supplementary Fig. S2G–S2N, vLung, vStomach, vPancreas, vBladder, vSkin, vOralM, vLarynx, vEsophagus). Remarkably, we found that the spatial separation of the FOLR2$^+$ TRMs (embedded in the adjacent benign tissue) and IL4I1$^+$ TAMs (located in and around tumor nests) was present in all tumors analyzed.

Our results suggest that spatially segregated macrophage populations may serve different functions. We show that FOLR2$^+$ TRMs are embedded in the normal tissue and are spatially segregated from IL4I1$^+$, NLRP3$^+$, and SPP1$^+$ macrophages, which are tumor associated. This is an important finding as revealing markers distinguishing TRMs from disease-associated macrophages is a crucial step that enables the study of individual macrophage subset functions and their relevance to disease progression (25).

IL4I1, FOLR2, LYVE1, and MARCO Label Spatially Segregated TRM Niches in Benign Colon and Breast

Next, we sought to learn whether the spatially segregated macrophage distribution we found in the TME was conserved in benign tissue. Previous reports have shown that TRMs govern tissue-specific roles driven by distinct gene expression programs in different normal tissues (8). Using our subset-specific markers, we found three distinct layers of TRMs in benign colon mucosa (Fig. 3A, left). Surprisingly, the IL4I1$^+$ macrophages, which we previously discovered to infiltrate tumor nests, were also present in the normal colon mucosa, where they localized at the top of the colon LP (luminal aspect). The second layer in the middle and bottom of the LP contained FOLR2$^+$ TRMs (Fig. 3B, v3B, NC1, NC2, NC4, NC6, NC7, NC8, NC9, NC12). The third TRM layer was localized in the colon submucosa and marked by FOLR2, LYVE1, and MARCO (Fig. 3C and D, v3C, v3D). As the gastrointestinal submucosa is rich in blood and lymph vessels, the submucosal FOLR2$^+$ LYVE1$^+$MARCO$^+$ TRM population likely corresponds to previously reported murine perivascular (PV) TRMs (26). The striking spatial segregation of TRMs in the bowel wall is consistent with the scRNAseq data that indicates the existence of two distinct FOLR2$^+$ TRMs populations: one that is positive for *FOLR2* alone (*FOLR2$^+$LYVE1$^-$ TRMs*) and one that coexpresses *FOLR2*, *LYVE1*, and *MARCOFOLR2$^+$LYVE1$^+$ TRMs*, Fig. 1D).

In comparison, we found two spatially segregated TRM populations in benign breast stroma. Consistent with a recent report (17), the TRMs surrounding benign breast lobules and ducts were FOLR2 positive (Fig. 3E, v3E). We called these cells lobular TRMs and found they express a low level of LYVE1 and MARCO (Fig. 3E and F i). Furthermore, we discovered that TRMs localized in the highly vascularized connective tissue that is further removed from the breast lobules coexpressed high levels of FOLR2, LYVE1, and MARCO (Fig. 3E and F ii, v3F).

Taken together, these results support the single-cell transcriptomic (Supplementary Fig. S1F) and mIHC (Fig. 2C and E–G) findings indicating that NLRP3$^+$ and SPP1$^+$ macrophages are associated with the TME, and FOLR2$^+$ and LYVE1$^+$ macrophages are located in normal tissues. Interestingly, we reveal the presence of IL4I1$^+$ macrophages in both normal colon and colorectal cancer, showing that they are present in both healthy and cancerous colon tissue.

IL4I1 Marks Phagocytosing Macrophages

IL4I1 localizes in the lysosomes of antigen-presenting cells (27), suggesting a role in phagocytosis. A close inspection of the IF-stained invasive front of colon tumor revealed the presence of pan-cytokeratin (CK)-positive granules within the cytoplasm of IL4I1$^+$ TAMs. We hypothesize that the pan-CK granules are apoptotic bodies derived from tumor cells that are being phagocytosed by the IL4I1$^+$ TAMs (Fig. 4A, v4A). The invasive front of the tumor is an area where intense tissue remodeling takes place. To invade the adjacent normal tissue, tumor cells need to make their way through the wall of tightly joined cells and the extracellular matrix. This process is likely to cause cell death and correlates with a rich presence of IL4I1$^+$ TAMs in the colorectal cancer invasive front. We also found that the IL4I1$^+$ macrophages on the top of the LP in normal colon, but not the FOLR2$^+$ TRMs in the middle and bottom of the crypt, contain apoptotic bodies of the intestinal epithelial cells (IEC; Fig. 4B, v4B, NC1p, NC2p, NC5p, NC6p, NC8p, NC10p, NC10.2p). This is consistent with the longstanding finding that macrophages ingest dying IEC at the top of the intestinal LP (28) but now provides a novel marker for the macrophage subset that executes this activity.

To further support the hypothesis that IL4I1 marks phagocytosing population of macrophages, we asked whether another specialized body phagocyte type, tingible body macrophages (TBMs), shows IL4I1 positivity. The TBMs localize in germinal centers where they remove apoptotic B cells (29) and thus are expected to have a high expression of phagocytic markers. TBMs contain apoptotic cellular debris at different degradation stages and are named after apoptotic nuclear debris ("tingible bodies") that can be observed in their cytoplasm. We found that the TBM in the LN germinal centers displayed very bright IL4I1 staining (Fig. 4C i, v4C) compared to the interfollicular macrophages that were FOLR2 positive (Fig. 4C ii). The presence of TBMs is also a hallmark of Burkitt's lymphoma, a tumor characterized by fast cell turnover (30). We examined two Burkitt's lymphoma cases and found that TBMs in this tumor display high IL4I1 expression (Fig. 4D, v4D).

We used gene set enrichment analysis to further investigate the association between phagocytosis and the IL4I1$^+$ TAMs. We found that compared to all other scRNA macrophage subtypes, the *CXCL9$^+$ TAMs* (a subset of *IL4I1$^+$ TAMs*) were most enriched in phagosome, lysosome, endocytosis, and antigen processing and presentation gene set expressions (Fig. 4E).

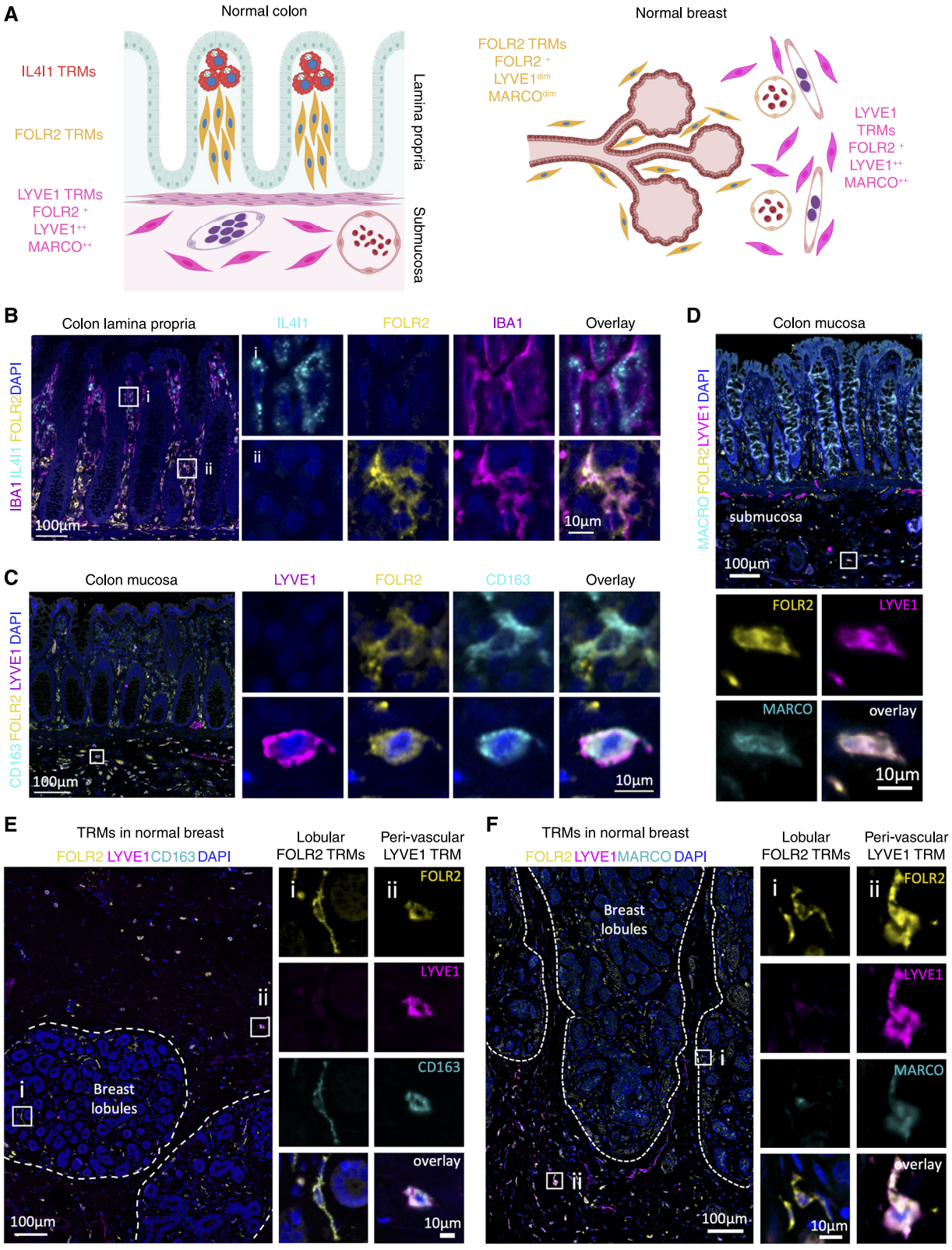

Figure 3. IL4I1, FOLR2, LYVE1, and MARCO label spatially segregated TRM niches in normal colon and breast. **A,** The schematic shows the distribution of TRM populations in normal colon mucosa and submucosa (left) and around normal breast glands (right). **B** and **C,** IF images show three TRM layers marked by IL4I1, FOLR2, and LYVE1 in normal colon mucosa and submucosa. Note that LYVE1 also stains normal lymph vessels. **D,** IF image shows that FOLR2$^+$, LYVE1$^+$ TRMs in normal colon submucosa are MARCO$^+$. **E** and **F,** IF images show TRMs in normal breast marked by FOLR2, LYVE1, and MARCO, depending on whether they are lobular (i) or PV (ii). **B–F,** Close-up images correspond to boxed regions. The scale bar of 10 µm is identical for all close-up images.

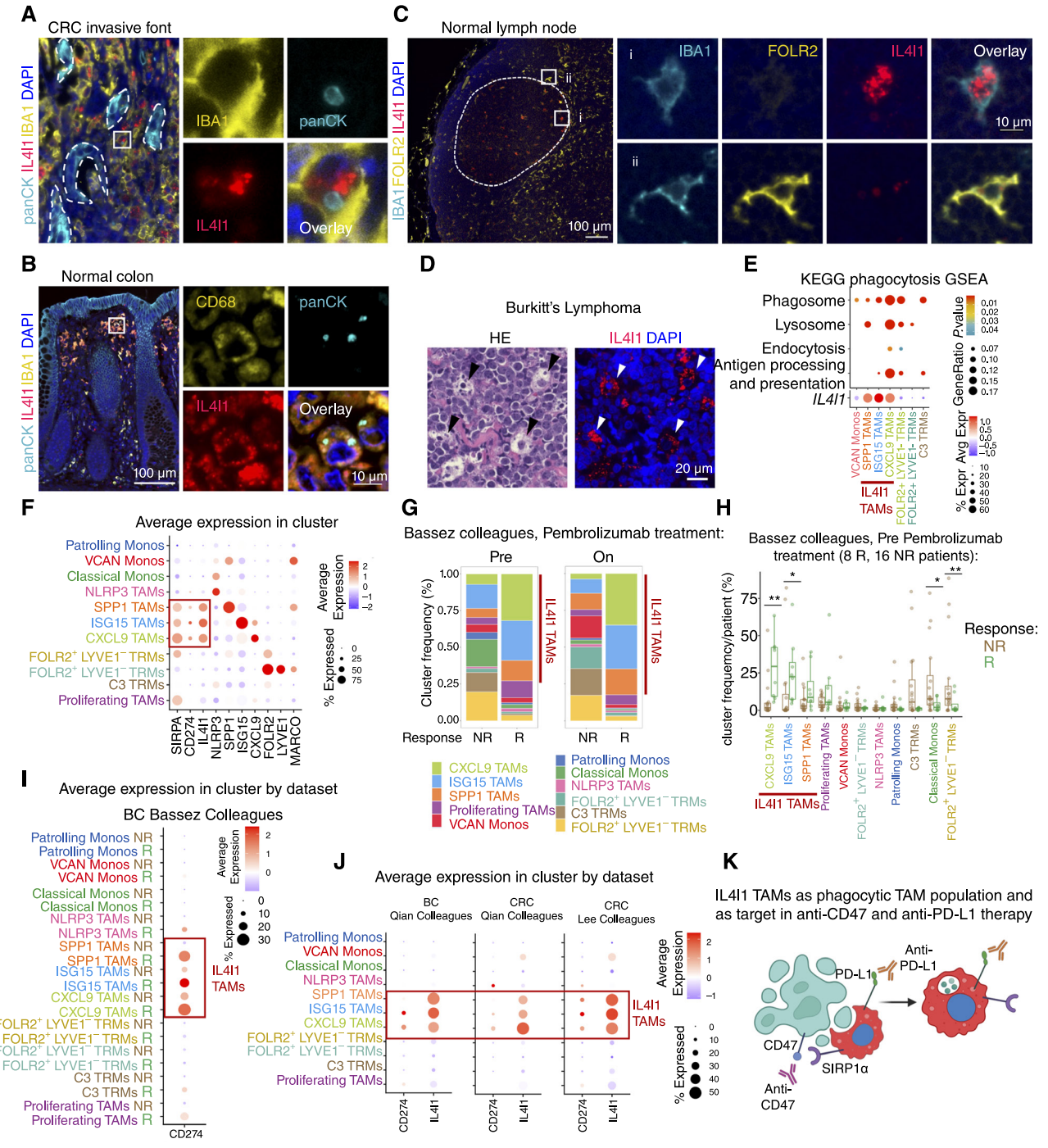

Figure 4. IL4I1 marks phagocytosing macrophages. **A,** IF images of invasive front of colorectal cancer stained with IL4I1, IBA1, panCK, and DAPI show the presence of panCK⁺ material within IL4I1 macrophages. **B,** Same as (**A**) but stained with IL4I1, CD68 and panCK in normal colon mucosa. **C,** IF images of normal Lymph node stained with IL4I1, FOLR2, IBA1, and DAPI. (i) is a close-up image of a germinal center TBM, (ii) is a close-up image of interfollicular FOLR2 TRMs. (**A–C**) Close-up images on the (right) correspond to the boxed region on the (left). **D,** Images of TBMs in Burkitt's lymphoma stained with left: H&E and right: IL4I1 and DAPI. **E,** Top: KEGG pathways enrichment analysis of phagocytosis-related pathways across scRNA macrophage populations. Populations with no significantly enriched pathways were omitted. Bottom: average IL4I1 gene expression across scRNA macrophage populations with enriched phagocytosis-related gene sets. **F,** Dotplot shows average gene expression in scRNA macrophage populations. **G,** Barplots show frequency of scRNA monocyte and macrophage clusters in dataset from Bassez and colleagues (23), stratified by response to pembrolizumab and time of sample collection. **H,** Boxplots show frequency of scRNA monocyte and macrophage clusters pre pembrolizumab treatment from Bassez and colleagues (23) (**I** and **J**) Same as **(F)** but from (**I**) Bassez and colleagues dataset (23), and (**J**) across Qian and colleagues (22) and Lee and colleagues (21) datasets. **K,** Schematic illustrating IL4I1 TAM association with cell death and efferocytosis and highlighting IL4I1 TAMs as potential anti-CD47 (indirect as IL4I1 TAMs express CD47 ligand-SIRP1α) and anti-PD-L1 (direct) therapy targets.

To evaluate the possible clinical relevance of this finding, we next asked whether *IL4I1*$^+$ *TAMs* express known phagocytosis checkpoints (like CD47 and PD-L1) and might thus be targets of phagocytosis-modulating cancer therapies, including anti-CD47 and anti-PD-L1 treatment (31). Indeed, using our integrated myeloid scRNAseq atlas (Fig. 1C), we found that *SIRPA* (which encodes the CD47 ligand) and *CD274* (encoding PD-L1) were both enriched in *IL4I1* expressing scRNA myeloid clusters, including *SPP1*$^+$ *TAMs*, *ISG15*$^+$ *TAMs*, and *CXCL9*$^+$ *TAMs* (Fig. 4F). In addition, we show that in comparison to all cells detected in the tissue, macrophages and mast cells are major sources of *CD274* in the TME (Supplementary Fig. S3A–S3D). Together, this indicates that of all macrophages present in the TME it is the IL4I1 TAMs that likely constitute an indirect target of anti-CD47 immunotherapies and a direct and major target of anti-PD-L1 immunotherapies.

Recent reports demonstrated that PD-L1 expression on TAMs, but not tumor cells, predicts response (32) and patient survival (33) in the context of patients receiving anti-PD-1/PD-L1 therapy. Thus, an important question is whether IL4I1 could be used as a predictive marker of response to PD-1 axis blockade. To address this question, we used the scRNA monocyte and macrophage transcriptomes from Bassez and colleagues (23) (Fig. 1C; Supplementary Fig. S1A) that contain samples of patients with advanced breast cancer taken before and after pembrolizumab treatment. We found that the frequency of IL4I1 expressing scRNA TAMs, both pretreatment and post-treatment, was increased in patients that responded to the therapy (Fig. 4G and H). This important finding suggests IL4I1 as a promising marker for response to PD-1 axis therapy.

In addition to their decreased frequency in the nonresponder group the *SPP1*$^+$ *TAMs*, *ISG15*$^+$ *TAMs*, and *CXCL9*$^+$ *TAMs* displayed decreased *CD274* gene expression compared to their counterparts in responders (Fig. 4I). Similar to IL4I1$^+$ transcriptional macrophages subsets in Bassez and colleagues dataset (23), the *SPP1*$^+$ *TAMs*, *ISG15*$^+$ *TAMs*, and *CXCL9*$^+$ *TAMs* from one breast and two separate scRNAseq colorectal cancer datasets displayed increased *CD274* gene expression compared to all other monocyte and macrophage subsets (Fig. 4J).

These results (i) demonstrate that IL4I1 is a marker associated with active phagocytosis of individual cells in breast cancer and colorectal cancer, (ii) suggest that IL4I1$^+$ TAMs are targets of the anti-CD47 and anti-PD-L1 immunotherapies (Fig. 4K) that may affect IL4I1$^+$ TAMs phagocytosis potential, and (iii) indicate IL4I1 as a potential novel predictive marker of PD1–PD-L1 axis blockade. Importantly, these results demonstrate that IL4I1$^+$ macrophage population is shared between healthy and diseased tissue with high cell turnover, including the top of the normal colon LP, germinal center TMB, Burkitt's lymphoma, and the TME.

CODEX Multiplexed Imaging Reveals Spatial Cellular Interactions in Macrophage Niches within Colon and Breast Cancer Tissues

Having identified the spatial segregation of the IL4I1, NLRP3, SPP1, FOLR2, and LYVE1 macrophage populations, we sought to elucidate the cellular compositions of the spatially segregated niches where these populations occur. We used CO-Detection by indEXing (CODEX) multiplexed tissue imaging to simultaneously visualize 36 protein markers on a single tissue microarray section of breast and colon benign and tumor tissue (34–36). This panel allowed us to recognize major immune, epithelial, and stromal cell types. Our CODEX antibody panel contained four general myeloid markers (CD16, CD68, CD163, CD206) and three macrophage subset-specific markers (SPP1, LYVE1, and FOLR2). Using the CODEX computational pipeline (i.e., imaging processing, single-cell segmentation, and unsupervised clustering; ref. 37), we identified two epithelial cell types, seven stromal cell types, and 15 immune cell types (Fig. 5A; Supplementary Fig. S4A). Among the immune cell types, we discriminated five macrophage populations: CD68$^+$ TAMs, SPP1$^+$ TAMs, CD163$^+$ TRMs, FOLR2$^+$ TRMs, and LYVE1$^+$ TRMs (Supplementary Fig. S4B). We could not add IL4I1, NLRP3, and MARCO antibodies to the CODEX panel for technical reasons. Based on their spatial tissue distribution (discussed below and illustrated in Supplementary Fig. S4C–S4E), the CODEX-identified CD68$^+$ TAMs likely corresponded to IL4I1$^+$ TAMs and NLRP3$^+$ TAMs populations we identified by IL4I1 and NLRP3 immunostaining in our IF studies using TMA sections immediately adjacent to the sections used for CODEX profiling (Fig. 2; Supplementary Fig. S5A). The CODEX-identified CD163$^+$ TRMs likely represent LYVE1$^+$ TRMs and FOLR2$^+$ TRMs for which FOLR2 and/or LYVE1 staining was not detected.

CODEX imaging showed that the distribution of CD68 and CD163 is different between the five macrophage populations, with CD68$^+$ and SPP1$^+$ TAMs enriched in CD68 expression while CD163$^+$, FOLR2$^+$, and LYVE1$^+$ TRMs were enriched in CD163 expression (Supplementary Fig. S4B). Consistent with the scRNAseq and four-color IF results (Figs. 1D and 3A, C–F), CODEX imaging confirmed the existence of two FOLR2-positive macrophage populations: FOLR2$^+$LYVE1$^-$ and FOLR2$^+$ LYVE1$^+$ (Supplementary Fig. S4B). Moreover, we validated that SPP1$^+$ TAMs (average distance 28.4 μm) localize more closely to tumor cells than FOLR2$^+$ macrophages (average distance 65.8 μm; Supplementary Fig. S4C). In addition, CODEX data showed that similar to FOLR2$^+$ TRMs, the CODEX LYVE1$^+$ TRMs are localized further away from the tumor (average distance 106 μm; Supplementary Fig. S4C). In agreement with our scRNAseq and IF analysis (Fig. 2B and D)—and in opposition to prior dogma—CD68$^+$ TAMs were again closer to the tumor nest than CD163$^+$ counterparts (Supplementary Fig. S4C).

To uncover the cellular composition of the different macrophage niches, we next performed cellular neighborhood analysis on the CODEX multiplexed imaging data (38–40). We clustered cells based on the identity of their 10 closest neighboring cells and identified 14 cellular neighborhoods, of which nine were enriched in macrophages (Fig. 5B). We grouped the nine macrophage-containing neighborhoods into four neighborhood types, each named after the primary macrophage subtype it contained: (i) a single CD68$^+$ TAM neighborhood, (ii) three SPP1$^+$ TAM neighborhoods, (iii) four FOLR2$^+$ TRM neighborhoods, and (iv) a single LYVE1$^+$ TRM neighborhood (Fig. 5B; Supplementary Fig. S4D). The single CD68$^+$ TAM neighborhood was localized inside the tumor nests and co-enriched with the tumor cells (Fig. 5B; Supplementary Fig. S5B, vS5B); we called it the intratumoral TAM neighborhood. The three discrete SPP1$^+$ TAMs neighborhoods were all enriched with SPP1$^+$

TAMs and the tumor cells but differed in cellular composition. The peritumoral SPP1$^+$ TAM neighborhood contained CD68 macrophages (Fig. 5B; Supplementary Fig. S5C, vS5C), the inflamed SPP1$^+$ TAM neighborhood contained neutrophils (Fig. 5B; Supplementary Fig. S5D, vS5D), and the hypoxic SPP1$^+$ TAM neighborhood held hypoxic tumor cells marked by CA9 expression (Fig. 5B; Supplementary Fig. S5E, vS5E). The four discrete FOLR2$^+$ neighborhoods were co-enriched in FOLR2$^+$ TRMs and CD163$^+$ TRMs but had different cell compositions and tissue locations. The plasma cell (PC) enriched FOLR2$^+$ TRM neighborhood was co-enriched with PCs and located close to the blood vessels and in the normal gastrointestinal (NGI) LP (Fig. 5B; Supplementary Fig. S5F, vS5F). The smooth muscle FOLR2$^+$ TRM neighborhood labeled the bowel muscle wall (Fig. 5B; Supplementary Fig. S5G, vS5G). The trapped fibrous FOLR2$^+$ TRM neighborhood was enriched in FAP fibroblasts and marked fibrous bands entrapped between growing tumor nests (Fig. 5B; Supplementary Fig. S5H, vS5H). The lymphoid FOLR2$^+$ TRM neighborhood contained CD4T, CD8T, Tregs, DCs, and FOLR2$^+$ TRMs (Fig. 5B; Supplementary Fig. S5I, vS5I). The LYVE1$^+$ TRM neighborhood was co-enriched with LYVE1$^+$ TRMs, FOLR2$^+$TRMs, CD163$^+$ TAMs, PDGFRβ fibroblasts, mast cells, and blood and lymph vessels. We called it the PV LYVE1 TRM neighborhood (Fig. 5B; Supplementary Fig. S5J, vS5J).

Next, we used two approaches to map each CODEX-macrophage neighborhood tissue distribution relative to the tumor. First, we computed the distance of every macrophage, labeled by the neighborhood it belongs to, to the closest tumor cell (Fig. 5C). Second, we calculated the fraction of tumor cells in every macrophage-enriched neighborhood (Fig. 5D). We interpret the distance to the tumor and the fractional enrichment in tumor cells as an indicator of how closely the given neighborhood is associated with the tumor. These analyses revealed remarkable spatial macrophage neighborhood segregation and a three-tier distribution of closeness to the tumor. Specifically, we show that TAMs in the hypoxic SPP1$^+$ neighborhood and the intratumoral neighborhood were located the closest to the tumor cells with an average distance of 9.37 and 10.6 μm to the nearest tumor cell (Fig. 5C) and that those two neighborhoods had the highest fraction of tumor cells (Fig. 5D). In contrast, TRMs in the lymphoid FOLR2$^+$, the PCs enriched FOLR2$^+$, the PV LYVE1$^+$ and the smooth muscle FOLR2$^+$ neighborhoods lay the farthest from the tumor with an average distance of 55.2, 57.5, 74.8, and 76.0 μm from the closest tumor cell (Fig. 5C). In agreement, they also contained the smallest percentage of tumor cells (Fig. 5D). Macrophages in the peritumoral SPP1$^+$, the inflamed SPP1$^+$, and the trapped fibrous FOLR2$^+$ neighborhoods localized at an intermediate distance between the two extremes.

To better visualize the spatial distribution of the macrophage neighborhoods in benign and tumor tissues, we plotted the neighborhood frequency by anatomic location. We show that the PV LYVE1$^+$ TRM neighborhood was most enriched in benign breast, while the PCs enriched FOLR2$^+$ TRM neighborhood was most enriched in NGI mucosa. The Smooth Muscle FOLR2$^+$ TRM neighborhood labels bowel wall and was thus specific to gut samples, and it could be detected in benign, in the invasive front and center of the tumor (CT) samples. This is consistent with the fact that colorectal cancer invades the bowel wall. In turn, the intratumoral TAM neighborhood, the inflamed SPP1$^+$ TAM neighborhood, the peritumoral SPP1$^+$ TAM neighborhood, the hypoxic SPP1$^+$ TAM neighborhood, and the trapped fibrous FOLR2$^+$ neighborhood were enriched in ductal carcinoma *in situ* (DCIS), invasive ductal carcinoma, in the IF of colorectal cancer and the colorectal cancer CT, further supporting that they are tumor associated (Fig. 5E; Supplementary Fig. S4E).

Taken together, the CODEX data (Fig. 5; Supplementary Figs. S4 and S5) allowed us to identify spatial associations between macrophage subtypes and other cell types in benign and tumor tissues. We showed that SPP1$^+$ TAMs were co-enriched with CD68$^+$ TAMs close to the tumor cells, localized in hypoxic tumor areas, and associated with neutrophilic infiltration. In contrast, CD163$^+$ TRMs, FOLR2$^+$ TRMs, and LYVE1$^+$ TRMs were co-enriched in adjacent benign tissue located further away from the tumor. We showed that FOLR2$^+$ TAMs constituted a tissue-resident macrophage population in the bowel muscle wall and were associated with PCs in the intestinal LP and connective breast tissue. We found that FOLR2$^+$ TRMs from the breast connective tissue or muscle bowel wall can be trapped within growing tumor nests and thus become a part of the TME (Fig. 5F).

FOLR2$^+$ TRMs Spatially Colocalize with Plasma Cells and May Maintain Long-Lived Plasma Cell Tissue Niche

To further explore the association between CODEX-identified FOLR2$^+$ TRM with PCs, we used IHC and multicolor IF. Single-color IHC showed that in the tumor-adjacent stroma FOLR2$^+$ TRMs were in direct contact with PCs, which can be histologically identified by their nuclear chromatin condensation pattern and asymmetric cytoplasmic "hof" where antibodies are produced and stored (arrowheads, Supplementary Fig. S6A). Multicolor IF additionally revealed that FOLR2$^+$ TRMs and CD38$^+$ PC occupied the same space in the middle and bottom layers of the colon LP (Supplementary Fig. S6B, vS6B), corroborating the CODEX results. Furthermore, we found Lobular FOLR2$^+$ TRMs were immediately adjacent to PCs around benign breast glands (Supplementary Fig. S6C, vS6C). Previous studies showed that CD163$^+$ macrophages surround PCs in the extrafollicular foci in the tonsil (41). Here we show that it was the FOLR2$^+$ TRM subtype that localized directly next to PCs in the LN interfollicular zone (Supplementary Fig. S6D, vS6D).

Figure 5. CODEX reveals spatial cellular interactions in macrophage niches within colon and breast cancer tissues. **A,** Schematic shows CODEX imaging and cellular neighborhood analysis workflow. **B,** Heatmap shows CODEX cell types (*x* axis) enrichment (color) in the identified cellular neighborhoods (*y* axis). **C,** Boxplot shows distance (μm) to the closest tumor cell for every macrophage identified by CODEX labeled by the neighborhood it belongs to. **D,** Barplot shows a percentage of the epithelial cells occupied in each CODEX macrophage neighborhood. **E,** Barplot presents the frequency of CODEX macrophage neighborhoods grouped by anatomical location. CT, center of tumor colorectal cancer; DCIS, ductal carcinoma *in situ* breast; IDC, invasive ductal carcinoma breast; IF, invasive front colorectal cancer; NB, normal breast; NGI, normal GI tract. **F,** Schematic shows cellular macrophage neighborhood organization and closeness to the tumor.

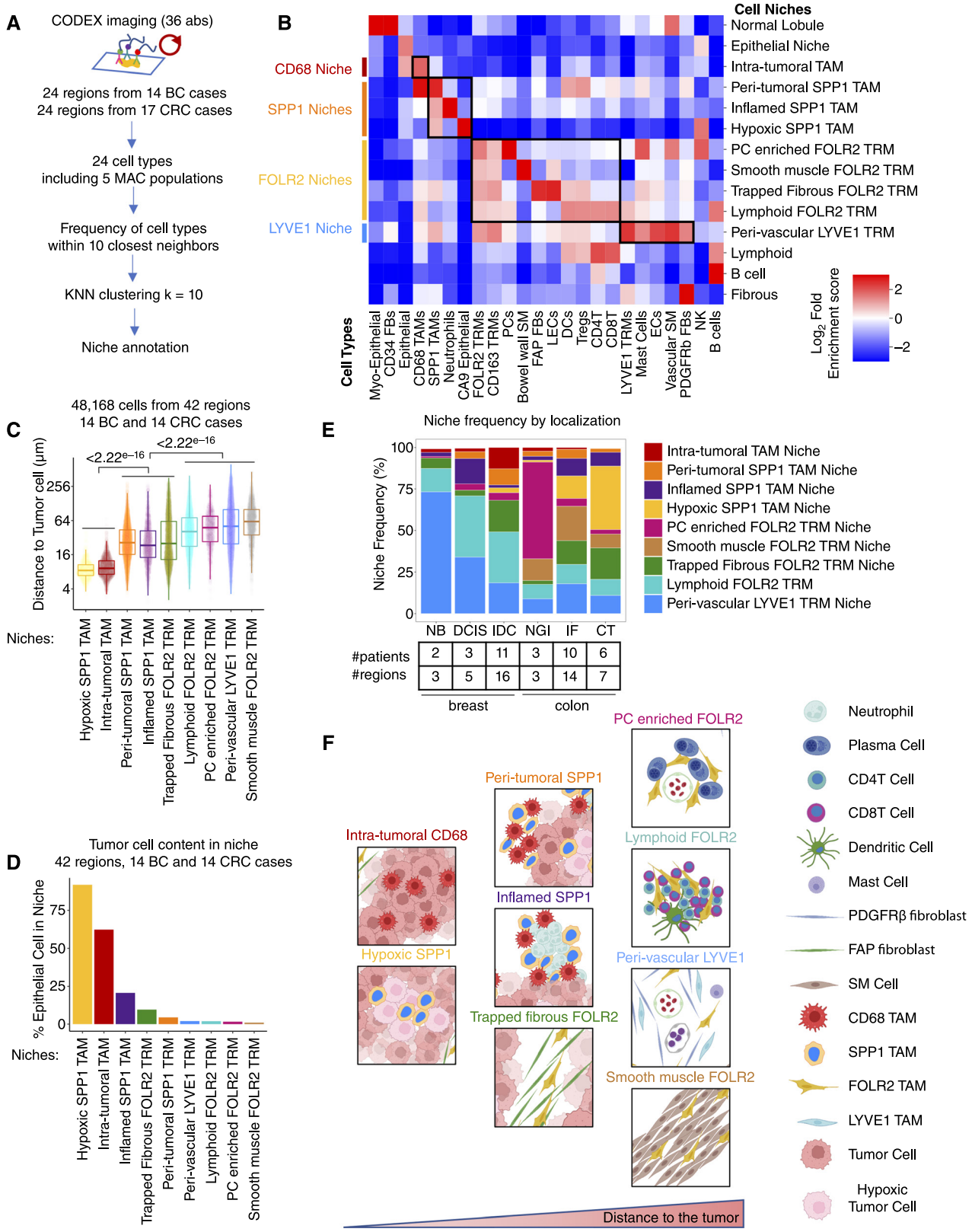
A
CODEX imaging (36 abs)
24 regions from 14 BC cases
24 regions from 17 CRC cases
24 cell types
including 5 MAC populations
Frequency of cell types
within 10 closest neighbors
KNN clustering k = 10
Niche annotation
B
CD68 Niche
SPP1 Niches
FOLR2 Niches
LYVE1 Niche
Cell Niches
Normal Lobule
Epithelial Niche
Intra-tumoral TAM
Peri-tumoral SPP1 TAM
Inflamed SPP1 TAM
Hypoxic SPP1 TAM
PC enriched FOLR2 TRM
Smooth muscle FOLR2 TRM
Trapped Fibrous FOLR2 TRM
Lymphoid FOLR2 TRM
Peri-vascular LYVE1 TRM
Lymphoid
B cell
Fibrous
Cell Types
Myo-Epithelial
CD34 FBs
Epithelial
CD68 TAMs
SPP1 TAMs
Neutrophils
CA9 Epithelial
FOLR2 TRMs
CD163 TRMs
PCs
Bowel wall SM
FAP FBs
LECs
DCs
Tregs
CD4T
CD8T
LYVE1 TRMs
Mast Cells
ECs
Vascular SM
PDGFRb FBs
NK
B cells
Log2 Fold Enrichment score
2
0
−2
C
48,168 cells from 42 regions
14 BC and 14 CRC cases
<2.22e−16
<2.22e−16
Distance to Tumor cell (µm)
256
64
16
4
Niches:
Hypoxic SPP1 TAM
Intra-tumoral TAM
Peri-tumoral SPP1 TAM
Inflamed SPP1 TAM
Trapped Fibrous FOLR2 TRM
Lymphoid FOLR2 TRM
PC enriched FOLR2 TRM
Peri-vascular LYVE1 TRM
Smooth muscle FOLR2 TRM
D
Tumor cell content in niche
42 regions, 14 BC and 14 CRC cases
% Epithelial Cell in Niche
75
50
25
0
Niches:
Hypoxic SPP1 TAM
Intra-tumoral TAM
Inflamed SPP1 TAM
Trapped Fibrous FOLR2 TRM
Peri-tumoral SPP1 TRM
Peri-vascular LYVE1 TRM
Lymphoid FOLR2 TRM
PC enriched FOLR2 TRM
Smooth muscle FOLR2 TRM
E
Niche frequency by localization
Niche Frequency (%)
100
75
50
25
0
Intra-tumoral TAM Niche
Peri-tumoral SPP1 TAM Niche
Inflamed SPP1 TAM Niche
Hypoxic SPP1 TAM Niche
PC enriched FOLR2 TRM Niche
Smooth muscle FOLR2 TRM Niche
Trapped Fibrous FOLR2 TRM Niche
Lymphoid FOLR2 TRM
Peri-vascular LYVE1 TRM Niche
NB DCIS IDC NGI IF CT
#patients 2 3 11 3 10 6
#regions 3 5 16 3 14 7
breast
colon
F
Intra-tumoral CD68
Peri-tumoral SPP1
PC enriched FOLR2
Lymphoid FOLR2
Inflamed SPP1
Hypoxic SPP1
Peri-vascular LYVE1
Trapped fibrous FOLR2
Smooth muscle FOLR2
Distance to the tumor
Neutrophil
Plasma Cell
CD4T Cell
CD8T Cell
Dendritic Cell
Mast Cell
PDGFRβ fibroblast
FAP fibroblast
SM Cell
CD68 TAM
SPP1 TAM
FOLR2 TAM
LYVE1 TAM
Tumor Cell
Hypoxic Tumor Cell

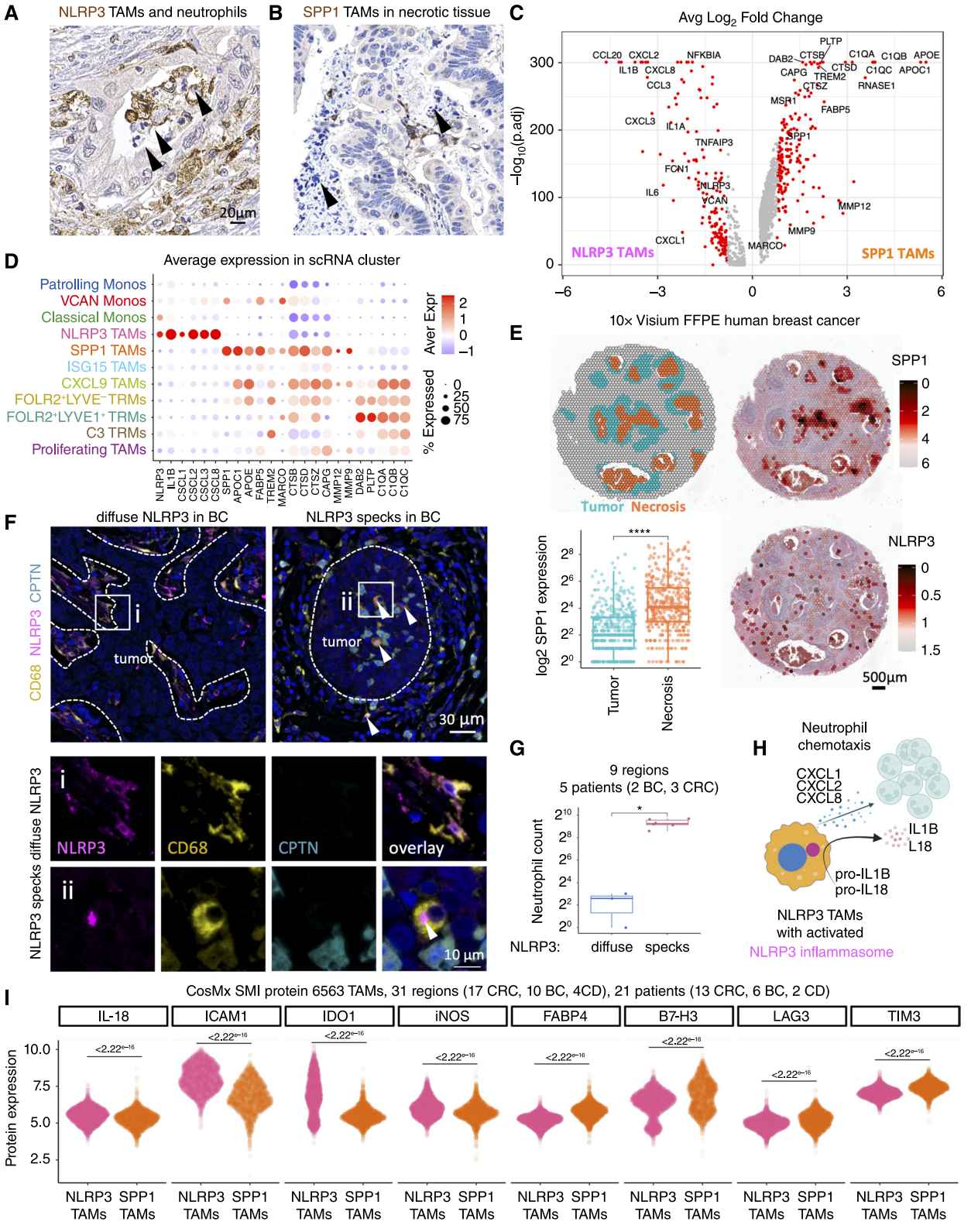

Figure 6. SPP1 TAMs are enriched in hypoxic and necrotic tumor areas and NLRP3 TAMs activate NLRP3 inflammasome in the TME. **A,** Immunohistochemical image shows NLRP3 TRMs surrounded by neutrophils (arrowheads). **B,** Immunohistochemical image shows SPP1 TRMs surrounded by karyorrhectic debris in necrotic material (arrowheads). **C,** Volcano plot shows differential gene expression between scRNA transcriptomes of SPP1 TAMs and NLRP3 TAMs. **D,** Dotplot of average expression of genes associated with neutrophil chemoattraction, lipid metabolism and phagocytosis across scRNA macrophage populations. **E,** Dotplot shows the annotation of tumor (green) and necrotic (brown) areas (top left) and normalized (*continued on next page*)

To unequivocally demonstrate that the cells spatially co-enriched with FOLR2$^+$ TRMs were PCs, we used 4-plex IF staining and showed that cells localized directly next to FOLR2$^+$ TRMs were marked by overlapping expression of CD38 and a prototypical PC marker—CD138 (Supplementary Fig. S6E, vS6E).

To demonstrate that the association between PCs and FOLR2$^+$ TRMs was specific, we computed the distance from every IL4I1$^+$ TAM and FOLR2$^+$ TRM to their closest PC across seven different tissue regions. As anticipated, PCs were localized closer to FOLR2$^+$ TRMs than the IL4I1$^+$ TAMs (Supplementary Fig. S6F and S6G).

To gain insight into the possible molecular mechanism governing the contact between the FOLR2$^+$ TRMs and PCs, we next performed scRNAseq-based ligand–receptor interaction analysis. In breast cancer (23), the highest probability interactions were found between APRIL (TNFSF13) and BAFF (TNFSF13B) on the *FOLR2$^+$ TRMs* and BCMA (TNFRSF17) on the *PCs* (Supplementary Fig. S6H). APRIL and BAFF are known to drive PC infiltration and their long-term survival in the tissue (42, 43). Similarly, using the *IgA$^+$PC*, *IgG$^+$PC*, and *FOLR2$^+$ TRMs* scRNAseq transcriptomes from benign colon and colorectal cancer (21), we also identified BAFF (TNFSF13B) and BCMA (TNFRSF17) interaction as the highest probability interaction between *IgA$^+$PC* and *FOLR2$^+$ TRMs* (Supplementary Fig. S6I). Our results provide a marker for the type of macrophage described in previous literature that suggests antigen-presenting cells maintain the PC niche in human tonsils (41), murine bone marrow (44), and human LP (45). These observations suggest that FOLR2$^+$ TRMs may play a key role in recruiting and maintaining PCs in inflamed benign tissue adjacent to tumors and the LP of benign colon (Supplementary Fig. S6J).

Prior work reported the existence of HES1$^+$/FOLR2$^+$ macrophages in normal human breast and lung, and human cancers of breast, liver, and lung (14, 17, 46). In addition, Chakarov and colleagues found LYVE1 expression to discriminate between two murine TRM populations, LYVE1^{lo} MHCII^{hi} CX3CR1^{hi} surrounding nerves, and LYVE1^{hi} MHCII^{lo} CX3CR1^{lo} surrounding the blood vessels (10). As mentioned above, the murine LYVE1^{hi} MHCII^{lo} CX3CR1^{lo} population likely corresponds to the FOLR2$^+$LYVE1$^+$ human macrophages we describe, as they display the same marker expression and share spatial tissue association with blood vessels. In contrast, the murine LYVE1^{lo} MHCII^{hi} CX3CR1^{hi} described by Chakarov and colleagues (10), and human FOLR2$^+$LYVE1$^-$ macrophages we describe here are not likely to correspond to each other as: (i) human FOLR2$^+$LYVE1$^-$ do not express *CX3CR1* gene (Fig. 1D) that was used by Chakarov and colleagues to define the murine LYVE1^{lo} MHCII^{hi} CX3CR1^{hi} population (10), and (ii) we find human FOLR2$^+$LYVE1$^-$ macrophages to spatially interact with plasma cells and not nerves (Fig. 5B; Supplementary Fig. S6). In fact, the murine LYVE1^{lo} MHCII^{hi} CX3CR1^{hi} population is more likely to correspond to the *C3$^+$ TRMs* subset we found in scRNAseq analysis since the *C3$^+$ TRMs* is the only macrophage subset expressing the *CX3CR1* gene (Fig. 1D). Therefore, our work significantly extends upon previous reports by showing that not one but two distinct FOLR2$^+$ TRM populations exist in humans, by providing a detailed topography of their distribution, and revealing their spatial cell interactions in human colon, breast, and lymph nodes that were not studied in mice. Importantly, we also, for the first time, revealed that a subset of FOLR2$^+$LYVE1$^-$ macrophages is embedded in the plasma cell tissue niche where it expresses signals promoting long-term plasma cell retention in the tissue.

SPP1$^+$ TAMs Are Enriched in Hypoxic and Necrotic Tumor Areas

CODEX neighborhood analysis revealed a spatial co-enrichment of SPP1 TAMs with neutrophils in the Inflamed SPP1$^+$ TAM niche. Notably, we also found NLRP3$^+$ TAMs to be enriched in neutrophil-infiltrated tumor areas (Fig. 6A). However, unlike NLRP3$^+$ TAMs, which were spatially co-enriched with live neutrophils in viable areas, SPP1$^+$ TAMs were associated with areas containing necrotic tissue (Fig. 6B). This observation prompted us to compare *NLRP3$^+$* and *SPP1$^+$ TAMs*' transcriptomes. Differential gene expression showed that *NLRP3$^+$ TAMs* expressed high levels of neutrophil chemoattractant cytokines (*CXCL1*, *CXCL2*, *CXCL8*). In contrast, the most upregulated genes in *SPP1$^+$ TAMs* were associated with phagocytosis and lipid metabolism, including apolipoproteins (*APOC1*, *APOE*), lipid scavenger receptors (*TREM2*, *MARCO*), lipid transporter *FABP5*, cathepsins (*CTSB*, *CTSD*, *CTSZ*), and matrix metalloproteinase (*MMP9*, *MMP12*; Fig. 6C and D). Interestingly, SPP1 itself has been implicated in phagocytosis (47, 48) and lipid metabolism (49). To further interrogate the association of SPP1$^+$ TAMs with necrosis, we used a publicly available 10× Visium FFPE Human Breast Cancer sample to show that necrotic tumor areas in this specimen were enriched in *SPP1$^+$* rather than *NLRP3$^+$* gene expression (Fig. 6E). These results suggest that NLRP3$^+$ TAMs likely contribute to neutrophil recruitment in the TME and that the SPP1$^+$ TAMs may play a role in the phagocytosis of necrotic tumor areas. It is important to note that although both IL4I1$^+$ TAMs and SPP1$^+$ TAMs are associated with phagocytosis and the SPP1$^+$ TAMs are a subset of IL4I1$^+$ TAMs, the IL4I1$^+$ macrophages are enriched in viable tissue areas with cells undergoing individual cell death, whereas the SPP1$^+$ TAMs are enriched in areas with large regions of hypoxic and necrotic tissue that is characterized by the presence of deceased neutrophils.

NLRP3$^+$ TAMs Activate NLRP3 Inflammasome in the TME

NLRP3 is a pathogen- and danger-associated molecular pattern receptor known to form an intracellular complex called the inflammasome, leading to proteolytic pro-IL1β

Figure 6. ***(Continued)*** expression of SPP1 (top right) and NLRP3 (bottom right) on the 10× Visium FFPE Human Breast Cancer sample, and barplot shows normalized $\log_2$ SPP1 expression in tumor and necrosis regions (bottom left). **F,** IF shows a representative breast cancer region stained with NLRP3, CD68, Calprotectin (CPTN), and DAPI. Scale bar of 10 μm is identical for all close-up images. **G,** Quantification of the number of neutrophils present on nine breast cancer 1.5 mm^2 tissue regions stratified by whether they contained diffuse NLRP3 (three regions) or NLRP3 specks (six regions). *P* value was computed using a two-sided Wilcoxon's rank-sum test. **H,** Schematic of a possible mechanism through which NLRP3 TAMs can contribute to the recruitment of neutrophils in the TME. **I,** Sina plots show marker protein expression profiled using CosMx SMI 64-plex Human Immuno-Oncology Protein Panel.

activation and release. IL1β is known to play a role in neutrophil recruitment in infection (50) and cancer (51). Inflammasome activation results in the assembly of proteins forming an inflammasome into a micrometer-sized protein complex called a speck (52). Speck formation can be used as a simple readout for inflammasome activation (53). Interestingly, we observed that in breast and colon cancer, the NLRP3 expression could be either seen as a diffuse expression within the macrophage cytoplasm (Fig. 6F i, v6Fi) or aggregated in a single speck (Fig. 6F ii, v6Fii). We found that speck-like NLRP3 aggregation, which we interpret as activated inflammasome complexes, was linked to neutrophil infiltration (Fig. 6F ii). To confirm, we stratified breast cancer and colorectal cancer NLRP3$^+$ TAM-positive regions by whether they were enriched in NLRP3$^+$ TAMs with diffuse staining or NLRP3$^+$ TAMs with NLRP3 specks, and quantified the number of neutrophils. The presence of NLRP3 specks in the cytoplasm of macrophages was associated with neutrophil tissue infiltration (Fig. 6G). Thus, we hypothesize that assembly of the inflammasome in NLRP3$^+$ TAMs likely induces IL1β activation and secretion, which drives neutrophil infiltration (Fig. 6H).

To extend our findings beyond cancer, we investigated whether we could detect NLRP3 inflammasome activation in CD, a type of inflammatory bowel disease associated with neutrophil infiltration. Indeed, the examination of three cases of advanced CD showed that regions with high macrophage infiltration (i) contained macrophages with NLRP3 specks and (ii) were highly infiltrated by neutrophils (Supplementary Fig. S7A and S7B, vS7B, CD2, CD3). The most convincing human studies implicating inflammasome involvement in human cancer are based on SNP associations and a report that IL1β blockade in atherosclerosis correlated with reduced incidence of lung cancer (54, 55). We are the first to provide histologic evidence demonstrating inflammasome formation in human breast cancer, colorectal cancer, and CD in human FFPE tissue sections and to demonstrate an association of the NLRP3 inflammasome formation with neutrophil infiltration.

To further validate the inflammatory properties of the NLRP3$^+$ TMAs in comparison to SPP1$^+$ TAMs, we profiled 31 0.5 mm^2 tissue regions (17 colorectal cancer, 10 breast cancer, 4 CD) across 21 patients (13 colorectal cancer, 6 breast cancer, 2 CD) using CosMx SMI 64-plex Human Immuno-Oncology Protein Panel. In support of proinflammatory polarization of the NLRP3$^+$ TAMs we found that they express significantly more proteins involved in tissue inflammation including IL-18, ICAM1, IDO1 and iNOS, compared to the SPP1$^+$ TAMs. In contrast, we found that the SPP1$^+$ macrophages express higher levels of immune-inhibitory receptors (B7-H3, LAG3, TIM3; Fig. 6I; Supplementary Fig. S7C and S7D, vS7Cl, vS7Cr, vS7Dl, vS7Dr).

Taken together, these results suggest that NLRP3$^+$ TAMs may be involved in the onset of inflammation by activating the NLRP3 inflammasome and may be driving neutrophil infiltration in human cancer and CD. In contrast, SPP1$^+$ TAMs seem to be playing a role in tissue repair by clearing necrotic lesions in hypoxic tumor areas.

High IL4I1$^+$ TAM Numbers Predict Good While High SPP1$^+$ TAM Numbers Predict Bad Patient Outcomes in Colorectal cancer

IF and scRNAseq studies of IL4I1$^+$ TAMs (Fig. 4A, E, and K) and SPP1$^+$ TAMs (Fig. 6C and D) suggest that both cell types perform phagocytosis in the TME. We next sought to elucidate the biological impact IL4I1$^+$ TAMs and SPP1$^+$ TAMs have on the tumor biology by correlating their abundance with clinical outcome in patients with colorectal cancer. Since scRNA-seq suggested that *IL4I1* is also expressed in SPP1$^+$ TAMs, we first stained for both IL4I1 and SPP1 simultaneously to learn to what extent the IL4I1 and SPP1 are co-expressed in a cell on the protein level (Fig. 7A–D, v7A). By analyzing 254 colorectal cancer regions from 135 patients we found that 56% of cells detected by IL4I1 and SPP1 staining were IL4I1 single positive (IL4I1$^+$ TAMs), 35% were SPP1 single positive (SPP1$^+$ TAMs), and 7% displayed a co-expression of IL4I1 and SPP1 (IL4I1$^+$SPP1$^+$ TAMs; Fig. 7B–D).

SPP1 and IL4I1 can be also expressed in epithelial cells, thus we stained with CD68, and IL4I1 or SPP1 antibodies simultaneously to quantify infiltration of IL4I1$^+$ TAMs and SPP1$^+$ TAMs in colorectal cancer (Fig. 7E and F, v7E, v7F). Previous reports showed that macrophage subtype signatures, including that of SPP1$^+$ TAM (13, 21, 56) and FOLR2$^+$ TRM (17), are predictive of clinical outcome in cancer. However, the association of IL4I1$^+$ TAMs with clinical outcomes remains unexplored and existing reports of SPP1$^+$ TAMs associations with outcome in colorectal cancer are based on RNA expression (13, 21). Since our data suggests that both IL4I1$^+$ TAMs and SPP1$^+$ TAMs are involved in tumor phagocytosis, we expected to see that high numbers of both TAM populations would be associated with favorable outcomes. This would be also in line with previous reports showing that CD68$^+$ macrophage infiltration in colorectal cancer is associated with a good outcome (4, 20). However, our analysis revealed that while IL4I1$^+$ TAMs are strong predictors of favorable outcome in two independent colorectal cancer cohorts (Fig. 7G and H; Supplementary Fig. S8A–S8D), the SPP$^+$ TAMs are associated with poor outcomes in colorectal cancer (Fig. 7I; Supplementary Fig. S8E and S8F). This is consistent with the spatial associations of SPP1$^+$ TAMs and tumor necrosis and hypoxia (Supplementary Figs. S5B, S5E, S6B, and S6E), and the fact that both tumor necrosis and hypoxia are hallmarks of tumor aggressiveness (57–59). To the best of our knowledge, this is the first protein-based evidence showing opposite

Figure 7. IL4I1 TAM infiltration predicts good and SPP1 TAM infiltration predicts bad outcome in colorectal cancer. **A,** IF image shows spatial distribution of SPP1 and IL4I1 staining in colorectal cancer. **B,** Heatmap shows normalized IF intensity in cells annotated as IL4I1 TAMs, SPP1 TAMs, and IL4I1$^+$SPP1$^+$ double-positive TAMs. **C–D,** Total proportion (**C**) and proportion by tissue region (**D**) of IL4I1 TAMs, SPP1 TAMs, and IL4I1$^+$SPP1$^+$ double-positive TAMs detected in 254 0.5 mm^2 tissue regions spanning 135 patients with colorectal cancer. **E,** IF image of a single tissue core from TA118 used for outcome analysis in (**H**), shows CD68 and IL4I1 protein expression in cells annotated as IL4I1 TAMs. **F,** IF image of a single-tissue core from TA118 used for outcome analysis in (**I**), shows CD68 and SPP1 protein expression in cells annotated as SPP1 TAMs. **G–I,** Kaplan–Meier plot of samples from patients with colorectal cancer stratified by normalized count of IL4I1 TAMs (**G** and **H**) or SPP1 TAMs (**I**). Presented are 40% (top) and 40% (bottom) cases.

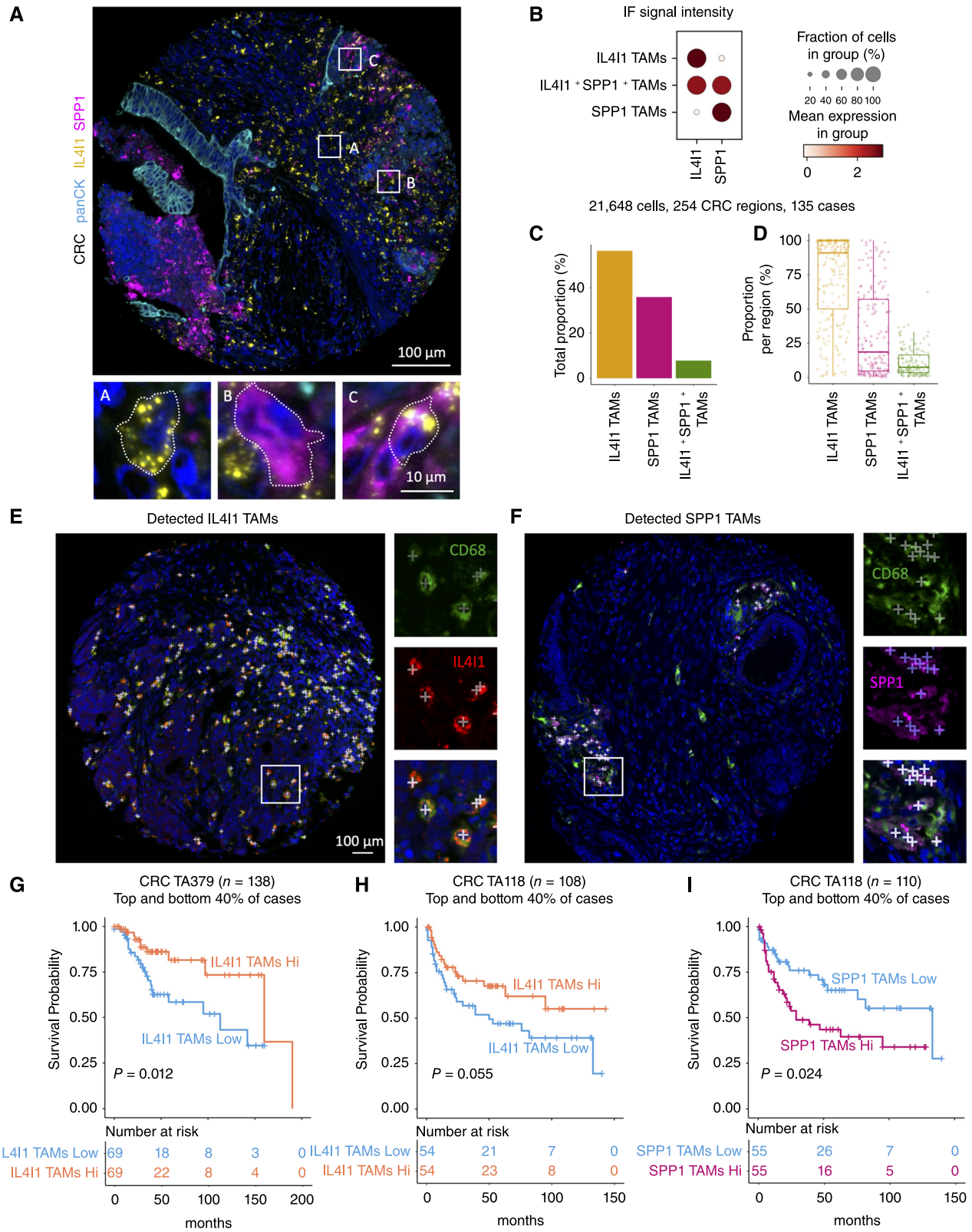
A
CRC panCK IL4I1 SPP1
C
A
B
100 μm
A
B
C
10 μm
B
IF signal intensity
IL4I1 TAMs
IL4I1 +SPP1 + TAMs
SPP1 TAMs
IL4I1
SPP1
Fraction of cells in group (%)
20 40 60 80 100
Mean expression in group
0 2
21,648 cells, 254 CRC regions, 135 cases
C
Total proportion (%)
0 20 40
IL4I1 TAMs
SPP1 TAMs
IL4I1 +SPP1 + TAMs
D
Proportion per region (%)
0 25 50 75 100
IL4I1 TAMs
SPP1 TAMs
IL4I1 +SPP1 + TAMs
E
Detected IL4I1 TAMs
CD68
IL4I1
100 μm
F
Detected SPP1 TAMs
CD68
SPP1
G
CRC TA379 (n = 138)
Top and bottom 40% of cases
Survival Probability
1.00 0.75 0.50 0.25 0.00
IL4I1 TAMs Hi
IL4I1 TAMs Low
P = 0.012
Number at risk
IL4I1 TAMs Low 69 18 8 3 0
IL4I1 TAMs Hi 69 22 8 4 0
0 50 100 150 200
months
H
CRC TA118 (n = 108)
Top and bottom 40% of cases
Survival Probability
1.00 0.75 0.50 0.25 0.00
IL4I1 TAMs Hi
IL4I1 TAMs Low
P = 0.055
Number at risk
IL4I1 TAMs Low 54 21 7 0
IL4I1 TAMs Hi 54 23 8 0
0 50 100 150
months
I
CRC TA118 (n = 110)
Top and bottom 40% of cases
Survival Probability
1.00 0.75 0.50 0.25 0.00
SPP1 TAMs Low
SPP1 TAMs Hi
P = 0.024
Number at risk
SPP1 TAMs Low 55 26 7 0
SPP1 TAMs Hi 55 16 5 0
0 50 100 150
months

clinical outcome correlations between two TAM populations in any solid tumor. This suggests a division of labor between different TAM populations, which may contribute differently to patient outcomes.

DISCUSSION

This work reveals a rich landscape of human macrophage populations, and their spatially segregated niches, conserved across healthy and cancerous human breast and colon tissue. These macrophage populations were not randomly distributed across the tissue; rather, each macrophage subset occupied a discrete multicellular niche. For example, we found IL4I1$^+$ macrophages are embedded in areas enriched in cell death in the desmoplastic stroma at the invasive front of the tumor across 10 different tumor types, in the upper LP of colonic mucosa, and in LN germinal centers. Thus, our findings indicate that macrophage populations, and the unique niches they occupy, are fundamental tissue "building blocks" reiteratively repeated within and across tissues. In addition, we uncover some of the incoming and outgoing signals governing the macrophage niche. For example, we are the first to histologically identify NLRP3 inflammasome aggregation in human cancer and to show that it is associated with neutrophil recruitment.

It has been recognized that TRMs across different organs exhibit specialized functions reflecting local tissue physiology (8). However, we are the first to uncover the existence of distinct functional spatial niches harboring discrete macrophage populations and cellular compositions within a single organ system in humans. In particular, we reveal the existence of four separate macrophage niches in the bowel wall, including a phagocytic IL4I1$^+$ TAM niche, a novel FOLR2$^+$ TRMs plasma cell niche, a PV LYVE1$^+$FOLR2$^+$ TRMs niche in the bowel submucosa, and a smooth muscle FOLR2$^+$ TRMs niche in the muscularis propria.

Notably, our results reveal that IL4I1$^+$, SPP1$^+$, and NLRP3$^+$ TAM niches are closely associated with tumor nests and implicated in the response to cancer, including individual tumor cell death, hypoxia and diffuse tissue necrosis, and acute inflammation, respectively. Surprisingly, we found opposite clinical outcome associations of IL4I1$^+$ TAMs and SPP1$^+$ TAMs in colorectal cancer: high IL4I1$^+$ TAM numbers are associated with better overall survival, whereas high SPP1$^+$ TAM numbers are associated with worse overall survival, hinting that these TAM populations might function dichotomously. Our results inform future TAM-directed immunotherapies, implying that targeting specific TAM populations might be therapeutically important, in contrast to current therapies that monolithically repress all TAMs.

In addition, IL4I1$^+$ TAMs might be implicated in response to anti-CD47 and anti-PD-L1 therapy as they express the CD47 ligand- *SIRPA* and *CD274* encoding PD-L1, and correlate with anti-PD1 treatment response. Moreover, we show that NLRP3 inflammasome activation correlates with acute inflammation in breast cancer, colorectal cancer, and CD. These findings nominate the NLRP3 inflammasome as a novel therapy target where its specific small molecule inhibitor—MCC950 (60) could function as a novel therapeutic agent in solid tumors and CD.

Collectively, our findings elucidate a landscape of discrete human macrophage niches, uncover unexpected cell interactions and mechanisms governing the macrophage niche biology, explore the prognostic and predictive significance, and suggest novel therapy targets (Supplementary Fig. S9). Importantly, as the antibody tools we present are FFPE-compatible, they enable the use of archival clinical material and provide a framework for the entire field to study human macrophage function in health and disease. All images acquired during this work are publicly accessible via an interactive browser (https://magdalenamat.github.io/Spatial_MAC_Map/), thus providing a resource for human macrophage research.

METHODS

Resource Availability

Lead Contact

Further information and requests for resources should be directed to and will be fulfilled by the lead contacts M. Matusiak (mmatusia@stanford.edu) and M. van de Rijn (mrijn@stanford.edu).

Materials Availability

This study did not generate new unique reagents.

Experimental Model and Subject Details

Human Patient Samples

All clinical specimens in this study were collected from patients with written informed consent for research use. The studies were conducted in accordance with the Declaration of Helsinki and approved by the Stanford University Institutional Review Board.

Breast and Colon Cohorts FFPE Samples. This study used FFPE samples from 36 invasive breast cancer (IBC) and 32 colon carcinoma (colorectal cancer) cases to identify differential spatial distribution of the FOLR2$^+$, LYVE1$^+$, IL4I1$^+$, SPP1$^+$, and NLRP3$^+$ macrophages in benign and malignant breast and colon tissue.

CD FFPE Samples. We performed the analysis in Fig. 6A and B, using three advanced FFPE samples from patients with CD.

Various Solid Tumor Samples. The images in Supplementary Fig. S2G–S2N were generated using a single FFPE case sample per indication.

IF and CODEX Tissue Microarrays. The tissue microarrays used in IF and CODEX experiments in this study were constructed from 36 1.5 mm^2 regions from 19 colorectal cancer cases, and 29 1.5 mm^2 regions from 18 IBC cases. Regions were selected based on differential spatial staining observed on full section staining with IL4I1, SPP1, and FOLR2 antibodies.

CosMx Tissue Microarray. The CosMx tissue microarray was constructed from 31 1 mm^2 tissue regions from 21 colorectal cancer, breast cancer and CD cases. Regions were selected based on differential spatial staining observed on full section staining with SPP1, NLRP3, IL4I1, and CD68 antibodies.

Method Details

External Datasets

Single-cell RNA-seq Tumor Atlases. Publicly available scRNA Seq datasets analyzed in this study are available under following links:

Qian and colleagues (22) and available under https://lambrechtslab.sites.vib.be/en/pan-cancer-blueprint-tumour-microenvironment-0, colorectal cancer data from Lee and colleagues (21) available in the NCBI Gene Expression Omnibus (GEO) database under the accession codes GSE132465, GSE132257, and GSE144735, and data from Bassez and colleagues (23) available at https://lambrechtslab.sites.vib.be/en/single-cell.

We obtained preprocessed scRNA-seq count data from four datasets covering breast carcinoma (breast cancer), and colon carcinoma (colorectal cancer). For each dataset, we extracted monocytes, macrophages, and dendritic cells by clustering SCTransformed count data using Seurat and subsetting clusters expressing *AIF1* (encoding IBA1), *CST3*, *CD68*, *CD163*, *ITGAX*, and *HLA-DRA*.

Next, we integrated the myeloid clusters from the four datasets using the reciprocal PCA workflow with Seurat. We used log normalization. To clean the data, we excluded dying cells, stressed cells, and cell duplets. We identified dying cells' clusters by inspecting the distribution of $\log_2$ (nCount_RNA + 1) per cell. Stressed cells were identified based on high expression levels of HSP genes. Cell duplets were identified based on the coexpression of non-myeloid cell markers as follows: myeloid-epithelial cell (*TFF3*, keratins), myeloid-Tcells (*CD3D*), myeloid-stromal cells (*SPARCL1*, *SPARC*, *COL1A1*), and myeloid-plasma (immunoglobulin genes). As we intended to focus exclusively on monocytes and macrophages, we excluded neutrophils and dendritic cell clusters identified based on the following gene enrichment: neutrophils (SOD2, GOS2, and low detected number of counts per cell), cDC1s (*CLEC9A*), cDC2s (*FCER1A*, *CD1C*, *CD1E*, and *CLEC10A*), migratoryDC (*BIRC3*, *CCR7*, *LAMP3*), follicular DC (*FDCSP* and immunoglobulin genes), plasmacytoid DC (*JCHAIN*, *LILRA4*, *IRF7*), CD207$^+$ DC (*CD1A*, *CD207*, *FCAR1A*). Next, we reclustered the integrated and cleaned Seurat object containing only monocytes and macrophages with resolution = 0.6 in the *FindClusters()* function. We obtained 15 clusters and annotated them based on the most differentially expressed genes in each cluster. Monocytes have been identified by *FN1*, *FCGR3A*, and *VCAN*. Macrophages were identified based on *C1QA*, *APOE*, and *TREM2* expression. We merged clusters 0 and 12 into ISG15 TAMs, clusters 1, 6, and 14 into CXCL9 TAMs, and clusters 11 and 13 into LYVE1$^+$FOLR2$^+$ TRMs. The resulting myeloid object is presented in Fig. 1C.

Spatial Transcriptomics. We obtained preprocessed spatial transcriptomic data from Human Breast Cancer: Ductal Carcinoma *In Situ*, Invasive Carcinoma (FFPE) sample data from 10x website https://www.10xgenomics.com/resources/datasets/human-breast-cancer-ductal-carcinoma-in-situ-invasive-carcinoma-ffpe-1-standard-1-3-0 (Fig. 6E).

Enrichment of Monocyte and Macrophage scRNA Seq Populations

For the analysis in Fig. 1F and Supplementary Fig. S1C–S1D, S1F, and S1G, we selected samples with more than 35 monocyte and macrophage cells and computed the frequency of the different scRNA subsets in each sample. Supplementary Figure S1C, S1D, and S1F, we present these frequencies stratified by tumor type and anatomical location. In addition, for Fig. 1F and Supplementary Fig. S1F, we computed a mean frequency for every scRNA subset and calculated a ratio of its frequency between breast cancer and colorectal cancer (Fig. 1F) and normal colon and colorectal cancer (Supplementary Fig. S1F).

Average Cluster Gene Expression

The average gene expression dotplots per scRNA monocyte and macrophage clusters in Figs. 1D, 2A, 4F, and 6D were plotted using the aggregated myeloid object from Fig. 1C.

Spatial Transcriptomics Dataset Processing and Visualization

For the analysis in Fig. 6E, we used STutility r package to normalize, annotate and visualize the pre-processed spatial transcriptomic data. Specifically, we used the SCTransform function for normalization and the ManualAnnotation function to annotate data based on the H&E image.

Immunohistochemistry

For the analysis in Supplementary Fig. S6A and Fig. 6A, B, 4 μm tissue sections were deparaffinized and rehydrated. Subsequently, antigen retrieval was performed in EDTA pH 9 buffer for 5 minutes at 95°C in a pressure cooker. Slides were next stained with FOLR2, SPP1, or NLRP3 antibodies listed in Supplementary Table S1, and imaged with a Keyence BZ-X800 microscope at 20′ magnification.

Immunofluorescence

For the analyses shown in Figs. 1G, 2D–G, 3B–F, 4A–D, 7A, E, F and Supplementary Figs. S2A–S2N, S6B–S6E, S6I, 6F, S7A, S7C, 4 μm full tissue sections were deparaffinized and rehydrated. Antigen retrieval was performed using EDTA pH 9 buffer at 95°C for 10 minutes. Sections were blocked for 20 minutes with horse serum and stained for 1 hour with primary antibodies. Sections were subsequently stained with secondary antibodies for 1 hour. A list of primary and secondary antibodies used in this work can be found in Supplementary Table S1. Sections were then mounted in ProLong Gold Antifade reagent with DAPI and cover-slipped. Stained sections were imaged with a Keyence BZ-X800 microscope at 20′ or 40′ magnification. Of note, LYVE1 is expressed on both TRMs and lymphatic endothelial cells. Yet, lymphatic endothelial cells can be readily differentiated from TRMs as they are organized in tubes, display much higher LYVE1 expression than TRMs, and do not express FOLR2 and MARCO (Fig. 3C, D, and F).

IF Images Dearraying

IF images were acquired with a Keyence BZ-X800 microscope at 20′ magnification. Next, the TMA core coordinates were extracted using the dearray functionality in QuPath (61). Subsequently, the TIFF TMA images were dearrayed using QuPath extracted core coordinates with vips crop function in Linux command line.

IF Images Cell Segmentation and IF Signal Quantification

Cell nuclei on the dearrayed TMA cores were segmented using Mesmer (62). Subsequently, IF signal was quantified for each detected nuclei by computing staining intensity within 3-pixel distance from the nuclear border. We consider a nucleus and its accompanying IF signal within 3-pixel distance from the nuclear border as a cell. In effect, each cell is described by its x and y pixel coordinate and IF staining intensity.

Clustering and Annotation of IF Data

Each individual IF staining was clustered separately. First, IF staining intensity was z normalized using z-score function from scipy.stats python module. Next, cells were clustered using Leiden clustering implementation in scanpy python package. All clusters were individually visually inspected on the dearrayed TIFF images by indicating location of cells attributed to a given cluster. Cell clusters were annotated based on morphology, location, and staining intensity.

For Supplementary Fig. S6C, we clustered and annotated cells form 7 1.5 mm^2 tissue regions including six breast cancer and one colorectal cancer cases. We used FOLR2, IL4I1, and CD138 staining intensity to discriminate FOLR2 TRMs, IL4I1 TAMs, and PCs, respectively.

Distance Quantification of IF and CODEX Data

For every TMA core, the distance between every cell and every other cell present in the core was computed using cdist function from scipy.spatial.distance python module. Next, for every macrophage, the shortest distance to a tumor cell was selected from the matrix of all cell distances. This shortest distance is reported as the distance to the closest tumor cell. For CODEX data, normal breast and gastrointestinal tract samples were excluded.

Significance Assessment within One Tissue Region. Wilcox test was used to assess the significance in Fig. 2D–G.

Significance Assessment Across Multiple Tissue Regions. Linear mixed-effect models were used to assess significance in Figs. 2B, C, 5C and Supplementary Figs. S4C, S6G.

We used the lmer function from package lme4 (v1.1.21), and took the tissue region intercept as a random effect. The pairwise *P*-values were derived from *t*-ratio statistics in the contrast analysis using the lmerTest (v3.1.2) and corrected for multiple hypotheses testing using the Holm Bonferroni method implemented in the modelbased (v0.1.2) package (github.com/easystats/modelbased).

CODEX Macrophage Distance Quantification by Niche

For distance quantification in Fig. 5C, macrophages were stratified by the macrophage niche they belong to.

CODEX Antibody Panel

The antibody panel in this study was constructed by selecting antibodies targeting epithelial and stromal tumor compartments, with a focus on the myeloid compartment. Detailed information on the included antibodies can be found in Supplementary Table S2. Each antibody was first conjugated to a unique oligonucleotide tag. Next, antibody-oligonucleotide conjugates were tested in low-plex fluorescence assay to determine whether their staining patterns match patterns established in IHC and IF experiments and to establish the best staining concentration and exposure time. Subsequently, all antibody conjugates were tested together in a single test CODEX imaging multicycle to evaluate optimal concentration, exposure time, and imaging cycle.

CODEX Imaging

CODEX imaging was performed as previously described (34). Breast cancer and colorectal cancer tissue microarrays were simultaneously stained with a previously validated cocktail of antibody-oligonucleotide conjugates and sequentially subjected to CODEX multiplexed imaging using the optimized conditions established during the test run. Metadata with detailed information on each CODEX run can be found in Supplementary Table S3.

CODEX Data Processing

CODEX imaging data was processed using a software tool called RAPID (Lu G and colleagues; manuscript under review, 2022), which included 3D GPU-based deconvolution, spatial drift correction, image stitching, and background subtraction (available at https://github.com/nolanlab/RAPID). Next, cell nuclei segmentation on the processed images was performed using a neural network-based segmentation algorithm called CellVisionSegmenter. CellVisionSegmenter has been shown to work well with segmenting both dense and diffuse cellular tissues with CODEX data (63). CellVisionSegmenter is an open-source, pre-trained nucleus segmentation and signal quantification software based on the Mask region-convolutional neural network (R-CNN) architecture. The only parameter that was altered was the growth pixels of the nuclear mask, which we found experimentally to work best at a value of 3.

CODEX Data Clustering, Visualization, and Cell Type Assignment

Cell clustering and annotation were performed according to a previously published protocol (37). First, nucleated cells were selected by subsetting cells with positive Hoechst signal imaged in two separate CODEX cycles. Next, marker signal intensity was *z*-normalized, and data was overclustered using Leiden clustering in scanpy Python package. Each cluster was visually examined by mapping a location of cells attributed to a given cluster to processed CODEX images and inspecting its marker staining. ImageJ was used to view processed CODEX images. Cell clusters were annotated based on cell morphology, tissue location, and marker staining intensity.

CODEX Niche Analysis

Niche analysis was performed as described earlier by Schürch and colleagues (38) with $k = 10$ nearest neighbors and 30 clusters. The cell clusters were annotated and grouped into 13 Niches based on location in the tissue and cell type enrichment score.

Ligand-Receptor Interaction Analysis

Ligan–receptor analysis was performed using CellChat R package workflow with default settings and using netVisual_bubble function to extract all identified significant liganr–receptor interactions between FOLR2 TRMs and plasma cells (PCs). For the analysis in Supplementary Fig. S6I, IgA^+ and IgG^+ PCs annotation was extracted from Lee and colleagues (21). For Supplementary Fig. S6H, PCs were identified using FindClusters Seurat function with res = 0.4, and selecting cluster #19 with high CD38 and JCHAIN expression. Supplementary Figure S6H shows all detected significant interactions between FOLR2 TRMs and PCs. Supplementary Figure S6I shows 10 top significant interactions detected between FOLR2 TRMs and IgA^+ and IgG^+ PCs.

Gene Set Enrichment Analysis

KEGG pathway gene set enrichment analysis from Fig. 4E was performed using clusterProfiler R package. The KEGG enrichment was performed on the list of differentially enriched genes between the 11 transcriptional MAC scRNA Seq populations. Next, enrichment results of antigen processing and presentation, phagosome, lysosome, and endocytosis gene sets were plotted to compare enrichment of phagocytosis-related pathways between the scRNA MAC populations.

Pembrolizumab Response Analysis

For the analysis in Fig. 4G and H, was performed on scRNA myeloid transcriptomes form Bassez and colleagues (23), that we created subsets from the aggregated myeloid object form Fig. 1C. The patient samples were stratified by the authors of the original publication based on whether the T cell repertoire, as assessed by TCR sequencing, expanded (E) or not (NE) after the pembrolizumab administration. We labeled patients with expanded T cell repertoire as responders (R) and patients with nonexpanded T cell repertoire as nonresponders.

For the analysis in Fig. 4H, we used scRNA monocyte and macrophage transcriptomes of responders and non-responders pre pembrolizumab treatment. We first computed scRNA cluster frequencies in patients with more than 35 monocyte and macrophage cells. Next we compared the mean scRNA cluster frequencies with chi-square test using chisq.test function from stats R package and used chisq.posthoc.test function from chisq.posthoc.test R package to assess significance. *P* values were adjusting using Bonferroni correction.

Neutrophil Infiltration Quantification in Breast Cancer, Colorectal Cancer, and CD

For the analysis in Fig. 6G, we counted the number of neutrophils present in 1.5 mm^2 TMA cores. The IF-stained TMA cores were evaluated by a pathologist and stratified into cores containing CD68

positive macrophages with diffuse NLRP3 staining or cores that contained CD68 positive macrophages with NLRP3 aggregated in a speck. Cores that contained both diffused and aggregated NLRP3 were classified as cores with NLRP3 speck, as we assumed that the NLRP3 aggregation contains an active inflammasome complex that projects the inflammatory signaling. For the analysis in Supplementary Fig. S7B, we counted the number of neutrophils in 1 mm^2 tissue regions selected from whole slide sections. We selected areas that contained CD68-positive macrophages containing NLRP3 aggregated in a speck. Since we did not detect any macrophages with NLRP3 diffuse staining in the CD tissue sections, we compared the neutrophil numbers in patients with CD to benign colon submucosa. CD68 and NLRP3 signals were used to identify NLRP3 TAMs, and calprotectin was used to identify neutrophils.

CosMx Protein Profiling

For the analysis in Fig. 6I and Supplementary Fig. S7D, CosMx protein data were produced by NanoString company as a service using the CosMx SMI 64-plex Human Immuno-Oncology Protein Panel. Images were processed and data generated using NanoString proprietary pipelines. Raw data were analyzed using Seurat package in R. Regions to profile were selected based on SPP1, NLRP3, and CD68 staining on the TMA section immediately adjacent to the section profiled in the CosMx assay (Supplementary Fig. S7C).

Survival Analyses

For the analyses in Fig. 7F–H and Supplementary Fig. S8, we stained two colorectal cancer tissue microarrays with a combination of CD68 and IL4I1 (TA118 and TA379), and CD68 and SPP1 (TA118). The IL4I1 TAM and SPP1 TAM counts detected on each tissue core were normalized by multiplying by 100 and dividing by the total cell number detected in each core. TA118 and TA379 contain two tissue cores per patient. For this analysis we selected a core with a higher number of detected total cells per core. Next we used R packages *survival* (v 3.5.3) and *survminer* (v 0.4.9) to fit and plot Kaplan–Meier survival curves. Survival curves were compared using the log-rank test.

Quantification and Statistical Analysis

Wilcoxon test was applied for group comparisons. Linear mixed effect models were applied when groups contained multiple observations from the same tissue region (for instance, when comparing the distance of macrophages to tumor cells across multiple tissue regions). Results with $P < 0.05$ were considered significant. Data analyses were performed with R and python. The investigators were not blinded to allocation during experiments and outcome assessment. No sample-size estimates were performed to ensure adequate power to detect a prespecified effect size.

Data Availability

All IF and CODEX images presented in the figures are available for viewing and download under https://magdalenamat.github.io/Spatial_MAC_Map/#/.

The myeloid scRNAseq object, CODEX and IF images, associated IF single cell data and annotations in tabular format, as well as all Python and R scripts used in this work can be found https://magdalenamat.github.io/Spatial_MAC_Map/#/files.

Interactive Histological Image Viewer

Our project's histological images, accessible via GitHub, can be investigated using an interactive image viewer we developed. This viewer is based on the OpenSeadragon Viewer, allowing high-resolution, deep-zoom image viewing. The user interface was constructed with Vue.js. All images were tiled to enable fast loading using the ImmunoViewer python package. Image data is hosted on the Google Cloud Platform. The viewer's source code is also available on our project's GitHub page: https://github.com/MagdalenaMat/Spatial_MAC_Map/tree/main/browser

Authors' Disclosures

M. Matusiak reports grants from NIH, and grants from D.K. Ludwig Fund for Cancer Research during the conduct of the study. M. van de Rijn reports grants from NIH during the conduct of the study. No disclosures were reported by the other authors.

Authors' Contributions

M. Matusiak: Conceptualization, resources, data curation, software, formal analysis, funding acquisition, validation, investigation, visualization, methodology, writing—original draft, project administration, writing—review and editing. **J.W. Hickey:** Resources, software, methodology, writing—review and editing. **D.G.P. van IJzendoorn:** Software. **G. Lu:** Resources. **L. Kidzinski:** Software. **S. Zhu:** Investigation. **D.R.C. Colburg:** Investigation. **B. Luca:** Software. **D.J. Phillips:** Resources. **S.W. Brubaker:** Resources. **G.W. Charville:** Resources. **J. Shen:** Resources. **K.M. Loh:** Writing—review and editing. **D.K. Okwan-Duodu:** Writing—review and editing. **G.P. Nolan:** Resources. **A.M. Newman:** Software, Writing—review and editing. **R.B. West:** Funding acquisition. **M. van de Rijn:** Conceptualization, funding acquisition, writing—original draft, writing—review and editing.

Acknowledgments

The authors would like to acknowledge S.H. Strand, J. Pollack, and K.D. Marjon for critical feedback on this work. This work was supported by grants from the National Cancer Institute (R.B. West and M. van de Rijn, R01CA229529), and the Virginia and D.K. Ludwig Fund for Cancer Research (M. van de Rijn). J.W. Hickey was supported by an NIH T32 Fellowship (T32CA196585), Cancer Research UK (C27165/A29073), and an American Cancer Society—Roaring Fork Valley Postdoctoral Fellowship (PF-20-032-01-CSM). G. Lu was supported by Stanford Cancer Institute (SCI) Innovation Award and by the National Cancer Institute of the National Institutes of Health under Award Number K99CA267171.

Note

Supplementary data for this article are available at Cancer Discovery Online (http://cancerdiscovery.aacrjournals.org/).

Received November 1, 2023; revised February 23, 2024; accepted March 26, 2024; published first March 27, 2024.

REFERENCES

1. Gordon S, Plüddemann A. Tissue macrophages: heterogeneity and functions. BMC Biol 2017;15:53.
2. DeNardo DG, Ruffell B. Macrophages as regulators of tumour immunity and immunotherapy. Nat Rev Immunol 2019;19:369–82.
3. Lazarov T, Juarez-Carreño S, Cox N, Geissmann F. Physiology and diseases of tissue-resident macrophages. Nature 2023;618:698–707.
4. Fridman WH, Zitvogel L, Sautès-Fridman C, Kroemer G. The immune contexture in cancer prognosis and treatment. Nat Rev Clin Oncol 2017;14:717–34.
5. Papadopoulos KP, Gluck L, Martin LP, Olszanski AJ, Tolcher AW, Ngarmchamnanrith G, et al. First-in-human study of AMG 820, a monoclonal anti-colony-stimulating factor 1 receptor antibody, in patients with advanced solid tumors. Clin Cancer Res 2017;23:5703–10.

6. Ries CH, Cannarile MA, Hoves S, Benz J, Wartha K, Runza V, et al. Targeting tumor-associated macrophages with anti-CSF-1R antibody reveals a strategy for cancer therapy. Cancer Cell 2014;25:846–59.
7. Lavin Y, Winter D, Blecher-Gonen R, David E, Keren-Shaul H, Merad M, et al. Tissue-resident macrophage enhancer landscapes are shaped by the local microenvironment. Cell 2014;159:1312–26.
8. Okabe Y, Medzhitov R. Tissue biology perspective on macrophages. Nat Immunol 2016;17:9–17.
9. Blériot C, Chakarov S, Ginhoux F. Determinants of resident tissue macrophage identity and function. Immunity 2020;52:957–70.
10. Chakarov S, Lim HY, Tan L, Lim SY, See P, Lum J, et al. Two distinct interstitial macrophage populations coexist across tissues in specific subtissular niches. Science 2019;363:eaau0964.
11. Domanska D, Majid U, Karlsen VT, Merok MA, Beitnes A-CR, Yaqub S, et al. Single-cell transcriptomic analysis of human colonic macrophages reveals niche-specific subsets. J Exp Med 2022;219: e20211846.
12. Azizi E, Carr AJ, Plitas G, Cornish AE, Konopacki C, Prabhakaran S, et al. Single-cell map of diverse immune phenotypes in the breast tumor microenvironment. Cell 2018;174:1293–308.e36.
13. Zhang L, Li Z, Skrzypczynska KM, Fang Q, Zhang W, O'Brien SA, et al. Single-cell analyses inform mechanisms of myeloid-targeted therapies in colon cancer. Cell 2020;181:442–59.e29.
14. Mulder K, Patel AA, Kong WT, Piot C, Halitzki E, Dunsmore G, et al. Cross-tissue single-cell landscape of human monocytes and macrophages in health and disease. Immunity 2021;54:1883–900.e5.
15. Cheng S, Li Z, Gao R, Xing B, Gao Y, Yang Y, et al. A pan-cancer single-cell transcriptional atlas of tumor infiltrating myeloid cells. Cell 2021;184:792–809.e23.
16. Luca BA, Steen CB, Matusiak M, Azizi A, Varma S, Zhu C, et al. Atlas of clinically distinct cell states and ecosystems across human solid tumors. Cell 2021;184:5482–96.e28.
17. Nalio Ramos R, Missolo-Koussou Y, Gerber-Ferder Y, Bromley CP, Bugatti M, Núñez NG, et al. Tissue-resident FOLR2$^+$ macrophages associate with CD8$^+$ T cell infiltration in human breast cancer. Cell 2022;185:1189–207.e25.
18. Kuppe C, Ramirez Flores RO, Li Z, Hayat S, Levinson RT, Liao X, et al. Spatial multi-omic map of human myocardial infarction. Nature 2022;608:766–77.
19. Qi J, Sun H, Zhang Y, Wang Z, Xun Z, Li Z, et al. Single-cell and spatial analysis reveal interaction of FAP$^+$ fibroblasts and SPP1$^+$ macrophages in colorectal cancer. Nat Commun 2022;13:1742.
20. Zhang Q-W, Liu L, Gong C-Y, Shi H-S, Zeng Y-H, Wang X-Z, et al. Prognostic significance of tumor-associated macrophages in solid tumor: a meta-analysis of the literature. PLoS One 2012;7:e50946.
21. Lee H-O, Hong Y, Etlioglu HE, Cho YB, Pomella V, Van den Bosch B, et al. Lineage-dependent gene expression programs influence the immune landscape of colorectal cancer. Nat Genet 2020;52:594–603.
22. Qian J, Olbrecht S, Boeckx B, Vos H, Laoui D, Etlioglu E, et al. A pan-cancer blueprint of the heterogeneous tumor microenvironment revealed by single-cell profiling. Cell Res 2020;30:745–62.
23. Bassez A, Vos H, Van Dyck L, Floris G, Arijs I, Desmedt C, et al. A single-cell map of intratumoral changes during anti-PD1 treatment of patients with breast cancer. Nat Med 2021;27:820–32.
24. Rőszer T. Understanding the mysterious M2 macrophage through activation markers and effector mechanisms. Mediators Inflamm 2015:2015:816460.
25. Park MD, Silvin A, Ginhoux F, Merad M. Macrophages in health and disease. Cell 2022;185:4259–79.
26. Lim HY, Lim SY, Tan CK, Thiam CH, Goh CC, Carbajo D, et al. Hyaluronan receptor LYVE-1-expressing macrophages maintain arterial tone through hyaluronan-mediated regulation of smooth muscle cell collagen. Immunity 2018;49:326–41.e7.
27. Mason JM, Naidu MD, Barcia M, Porti D, Chavan SS, Chu CC. IL-4-induced gene-1 is a leukocyte L-amino acid oxidase with an unusual acidic pH preference and lysosomal localization. J Immunol 2004;173:4561–7.
28. Nagashima R, Maeda K, Imai Y, Takahashi T. Lamina propria macrophages in the human gastrointestinal mucosa: their distribution, immunohistological phenotype, and function. J Histochem Cytochem 1996;44:721–31.
29. Aguzzi A, Kranich J, Krautler NJ. Follicular dendritic cells: origin, phenotype, and function in health and disease. Trends Immunol 2014;35:105–13.
30. Gotur SP, Wadhwan V. Tingible body macrophages. J Oral Maxillofac Pathol 2020;24:418–20.
31. Gordon SR, Maute RL, Dulken BW, Hutter G, George BM, McCracken MN, et al. PD-1 expression by tumour-associated macrophages inhibits phagocytosis and tumour immunity. Nature 2017;545:495–9.
32. Li H, van der Merwe PA, Sivakumar S. Biomarkers of response to PD-1 pathway blockade. Br J Cancer 2022;126:1663–75.
33. Liu Y, Zugazagoitia J, Ahmed FS, Henick BS, Gettinger SN, Herbst RS, et al. Immune cell PD-L1 colocalizes with macrophages and is associated with outcome in PD-1 pathway blockade therapy. Clin Cancer Res 2020;26:970–7.
34. Black S, Phillips D, Hickey JW, Kennedy-Darling J, Venkataraaman VG, Samusik N, et al. CODEX multiplexed tissue imaging with DNA-conjugated antibodies. Nat Protoc 2021;16:3802–35.
35. Kennedy-Darling J, Bhate SS, Hickey JW, Black S, Barlow GL, Vazquez G, et al. Highly multiplexed tissue imaging using repeated oligonucleotide exchange reaction. Eur J Immunol 2021;51:1262–77.
36. Goltsev Y, Samusik N, Kennedy-Darling J, Bhate S, Hale M, Vazquez G, et al. Deep profiling of mouse splenic architecture with CODEX multiplexed imaging. Cell 2018;174:968–81.e15.
37. Hickey JW, Tan Y, Nolan GP, Goltsev Y. Strategies for accurate cell type identification in CODEX multiplexed imaging data. Front Immunol 2021;12:727626.
38. Schürch CM, Bhate SS, Barlow GL, Phillips DJ, Noti L, Zlobec I, et al. Coordinated cellular neighborhoods orchestrate antitumoral immunity at the colorectal cancer invasive front. Cell 2020;182:1341–59.e19.
39. Phillips D, Matusiak M, Gutierrez BR, Bhate SS, Barlow GL, Jiang S, et al. Immune cell topography predicts response to PD-1 blockade in cutaneous T cell lymphoma. Nat Commun 2021;12:6726.
40. Jiang S, Chan CN, Rovira-Clavé X, Chen H, Bai Y, Zhu B, et al. Combined protein and nucleic acid imaging reveals virus-dependent B cell and macrophage immunosuppression of tissue microenvironments. Immunity 2022;55:1118–34.e8.
41. Xu W, Joo H, Clayton S, Dullaers M, Herve M-C, Blankenship D, et al. Macrophages induce differentiation of plasma cells through CXCL10/IP-10. J Exp Med 2012;209:1813–23, S1–2.
42. Kawakami T, Mizushima I, Yamada K, Fujii H, Ito K, Yasuno T, et al. Abundant a proliferation-inducing ligand (APRIL)-producing macrophages contribute to plasma cell accumulation in immunoglobulin G4-related disease. Nephrol Dial Transpl 2019;34:960–9.
43. Benson MJ, Dillon SR, Castigli E, Geha RS, Xu S, Lam K-P, et al. Cutting edge: the dependence of plasma cells and independence of memory B cells on BAFF and APRIL. J Immunol 2008;180:3655–9.
44. Rozanski CH, Arens R, Carlson LM, Nair J, Boise LH, Chanan-Khan AA, et al. Sustained antibody responses depend on CD28 function in bone marrow-resident plasma cells. J Exp Med 2011;208:1435–46.
45. Hickey JW, Becker WR, Nevins SA, Horning A, Perez AE, Zhu C, et al. Organization of the human intestine at single-cell resolution. Nature 2023;619:572–84.
46. Sharma A, Seow JJW, Dutertre C-A, Pai R, Blériot C, Mishra A, et al. Onco-fetal reprogramming of endothelial cells drives immunosuppressive macrophages in hepatocellular carcinoma. Cell 2020;183: 377–94.e21.
47. Shin Y-J, Kim HL, Choi J-S, Choi J-Y, Cha J-H, Lee M-Y. Osteopontin: correlation with phagocytosis by brain macrophages in a rat model of stroke. Glia 2011;59:413–23.
48. Schack L, Stapulionis R, Christensen B, Kofod-Olsen E, Skov Sørensen UB, Vorup-Jensen T, et al. Osteopontin enhances phagocytosis through a novel osteopontin receptor, the alphaXbeta2 integrin. J Immunol 2009;182:6943–50.
49. Remmerie A, Martens L, Thoné T, Castoldi A, Seurinck R, Pavie B, et al. Osteopontin expression identifies a subset of recruited macrophages distinct from Kupffer cells in the fatty liver. Immunity 2020;53:641–57.e14.

50. Miller LS, Pietras EM, Uricchio LH, Hirano K, Rao S, Lin H, et al. Inflammasome-mediated production of IL-1beta is required for neutrophil recruitment against *Staphylococcus aureus in vivo*. J Immunol 2007;179:6933–42.
51. Chen L-C, Wang L-J, Tsang N-M, Ojcius DM, Chen C-C, Ouyang C-N, et al. Tumour inflammasome-derived IL-1β recruits neutrophils and improves local recurrence-free survival in EBV-induced nasopharyngeal carcinoma. EMBO Mol Med 2012;4:1276–93.
52. Lamkanfi M, Dixit VM. Mechanisms and functions of inflammasomes. Cell 2014;157:1013–22.
53. Stutz A, Horvath GL, Monks BG, Latz E. ASC speck formation as a readout for inflammasome activation. In: De Nardo CM, Latz E, editors. The inflammasome: methods and protocols. Totowa, NJ: Humana Press; 2013. p. 91–101.
54. Ridker PM, MacFadyen JG, Thuren T, Everett BM, Libby P, Glynn RJ, et al. Effect of interleukin-1β inhibition with canakinumab on incident lung cancer in patients with atherosclerosis: exploratory results from a randomised, double-blind, placebo-controlled trial. Lancet 2017;390:1833–42.
55. Sharma BR, Kanneganti T-D. NLRP3 inflammasome in cancer and metabolic diseases. Nat Immunol 2021;22:550–9.
56. Bill R, Wirapati P, Messemaker M, Roh W, Zitti B, Duval F, et al. *CXCL9:SPP1* macrophage polarity identifies a network of cellular programs that control human cancers. Science 2023;381:515–24.
57. Lam JS, Shvarts O, Said JW, Pantuck AJ, Seligson DB, Aldridge ME, et al. Clinicopathologic and molecular correlations of necrosis in the primary tumor of patients with renal cell carcinoma. Cancer 2005;103:2517–25.
58. Swinson DEB, Jones JL, Richardson D, Cox G, Edwards JG, O'Byrne KJ. Tumour necrosis is an independent prognostic marker in non-small cell lung cancer: correlation with biological variables. Lung Cancer 2002;37:235–40.
59. Fisher ER, Anderson S, Redmond C, Fisher B. Pathologic findings from the National Surgical Adjuvant Breast Project protocol B-06. 10-year pathologic and clinical prognostic discriminants. Cancer 1993;71:2507–14.
60. Coll RC, Robertson AAB, Chae JJ, Higgins SC, Muñoz-Planillo R, Inserra MC, et al. A small-molecule inhibitor of the NLRP3 inflammasome for the treatment of inflammatory diseases. Nat Med 2015;21:248–55.
61. Bankhead P, Loughrey MB, Fernández JA, Dombrowski Y, McArt DG, Dunne PD, et al. QuPath: open source software for digital pathology image analysis. Sci Rep 2017;7:16878.
62. Greenwald NF, Miller G, Moen E, Kong A, Kagel A, Dougherty T, et al. Whole-cell segmentation of tissue images with human-level performance using large-scale data annotation and deep learning. Nat Biotechnol 2022;40:555–65.
63. Lee MY, Bedia JS, Bhate SS, Barlow GL, Phillips D, Fantl WJ, et al. CellSeg: a robust, pre-trained nucleus segmentation and pixel quantification software for highly multiplexed fluorescence images. BMC Bioinformatics 2022;23:46.